UNIVERSITÀ DEGLI STUDI DI MESSINA

DIPARTIMENTO DI SCIENZE MATEMATICHE E INFORMATICHE,
SCIENZE FISICHE E SCIENZE DELLA TERRA

Dottorato di Ricerca in Fisica

SSD FIS/04

Characterization of GET Electronics coupled to the CHIMERA and FARCOS multi-detectors for nuclear reaction studies

Tesi di:

Saverio De Luca

Tutor:

Prof. Antonio Trifirò

Co-tutor:

Dott. Giuseppe Cardella

XXIX CICLO

TRIENNIO 2014-2016

A Ketty.

Introduction

Studying the equation of state (EoS) of asymmetric nuclear matter represents one of the main goals in nuclear physics research [1]. The EoS is determined by the details of in-medium nuclear interaction and plays a key role in determining the properties of astrophysical objects, such as neutron stars and supernovae explosions [2].
Accessing information on the interaction between neutrons and protons in a dilute and hot environment similar to that existing in stars is however difficult and one is forced to rely on measurements from astrophysical observations and nuclear reactions studied at accelerator facilities. In this kind of reactions, a high number of fragments are produced and it is important to identify them in a wide range of energy, mass and angles.
For this reason in the late 1990s at LNS (Laboratori Nazionali del Sud) of Catania the 4π multi-detector CHIMERA (Charged Heavy Ion Mass and Energy Resolving Array) was designed and constructed [3]. CHIMERA is equipped with electronics in discrete components that, also through analysis in the form of the signal produced by detected particles, allows a recognition of fragments in change and/or mass in a wide dynamic range [4].
This detector is still very powerful. Part of its electronics (for the Silicon stage) has been recently updated, however it needs some further improvement.
From the point of view of physics cases, a large number of investigations performed in heavy-ion collision reaserches are now based on two- and multi-particle correlation measurements. These measurements require high angular and energy resolution, especially focused on the detection of light particles abundantly produced during the overall dynamical evolution of excited and dilute nuclear systems produced in central and peripheral impacts. To im-

prove CHIMERA response function for these cases a new array, FARCOS, has been studied and is going to be built.
The present work is devoted to study and characterization of the compact GET electronics, that must be used for both the final FARCOS array, constituted by 20 telescopes (about 2600 detectors) and the 4π CHIMERA CsI(Tl) (1192 detectors) front-end, now obsolete. Our choice was to develop a first stage front-end circuit for FARCOS (including new ASIC pre-amplifiers) and new dual-gain modules coupled to a compact hardware architecture covering digitalization and signal readout, synchronization and trigger functions. These last aspects are covered by the GET project.
With the compact GET electronics we have large advantages respect to old electronics based on discrete components, for example few racks will be enough for all FARCOS and CHIMERA (CsI detectors) electronics and we will use only $5\,W$ for 256 channels, so the total power consumption will be much lower than the present (for CHIMERA we need now about 60 kW of power in 10 racks).
The new electronics is fully digital so allowing the complete storage of the detector signals with obvious advantages for the pulse shape analysis and noise rejection. Moreover, the compactness of this electronics allows us to transport it easily.
The PhD thesis is organized in four chapters.

In chapter 1, first of all it is described the physics cases, with a general introduction to the different "correlation methods". Then both FARCOS project and the choice of GET electornics are described. After, a comparison between the analog electronics and digital one is made. Finally a description of software filters, that we use for online and offline analysis, is described.

In chapter 2, the construction details of CHIMERA, FARCOS-PROTOTYPE and GET electronics are described. Moreover, the Dual Gain Module (necessary for double dynamic range) and identification methods developed by using such electronics are described.

In chapter 3, the results of the performed tests with radioactive sources and with internal and external pulser are described.

Finally, chapter 4 is devoted to results obtained during on beams experiment are reported. A final paragraph reports the perspectives using the new electronics.

Contents

Chapter 1

Physics cases and experimental techniques

1.1 Physics cases

In heavy-ion collisions at intermediate energies (from 20 to 200 $AMeV$) the nuclei are exposed to a violent collective compression phase where the overlapping nuclear matter is predicted to reach values of density well above the saturation value $\rho_0 = 0.17\, nucleon/fm^3$.
The following expansion phase brings the density down to significant low values, the so-called freeze-out phase ($\rho \sim 0.3\,\rho_0$), which turns up in the multi-fragmentation phase where many excited clusters and light particles are ejected from the collision center.

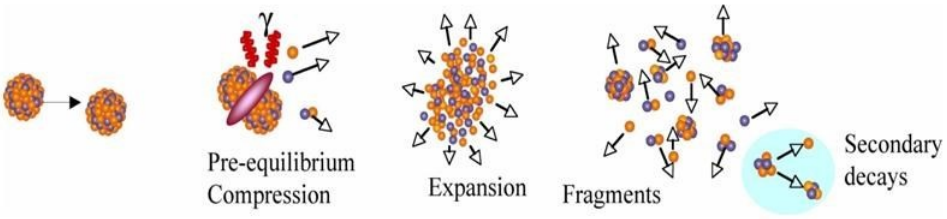

Figure 1.1: Representation of the time evolution of a heavy-ion collision with highlighted the different reaction phases. To give an idea of the time scale of the process, the freeze-out phase (fragment ejection) occurs some $10^{-22}\,s$ after the beginning of the collision.

Figure 1.1 shows a representation of the time evolution of a heavy-ion collision, highlighting the different reaction phases. If on one side, there is still not the certainty whether the system schieves full equilibrium in the freeze-out phase, on the other there are clear evidences of the presence of secondary decays from emitted fragments.
This complex scenario can be investigated with the powerful techniques of intensity interferometry and correlation functions [5]. Correlation functions at small relative momentum allow measurements of the order of magnitude of $10^{-15}\,m$ for spatial dimensions and of $10^{-23} \div 10^{-20}\,s$ for time intervals [6]. Despite this great achievement, one of the fundamental problems is to disentangle the prompt emitting sources from secondary emitting ones whose characteristic time scales are order of magnitude greater.
The difficulty is even magnified by the extrem sensitivity to parameters such as beam energy, the centrality of the collision (impact parameter) and the mass of the system [5]. Nevertheless, a suitable gating of impact parameters, reaction plane, charged particle multiplicity and other global parameters comes in partial aid to decipher the several emitting source components [7].
Proton-proton correlation function is the most common technique exploited in *Hanbury-Brown-Twiss* (HBT) intensity interferometry studies. It is defined as follow

$$Y_{12}(\vec{p_1}, \vec{p_2}) = c_{12} \cdot (1 + R_{\vec{p}}(\vec{q}))Y_1(\vec{p_1})Y_2(\vec{p_2}) \tag{1.1}$$

where $Y_{12}(\vec{p_1}, \vec{p_2})$ is the yield of the two coincident particles detected at the same event, C_{12} is a normalization constant obtained by imposing $R_{\vec{p}}(\vec{q}) = 0$ for very large value of relative momentum $\vec{q}$ of the particles, $Y_1(\vec{p_1})$ and $Y_2(\vec{p_2})$ are the yields of the single particles, $\vec{p}$ is the total momentum of the pair and $1 + R_{\vec{p}}(\vec{q})$ is the proton-proton correlation function.
Thanks to the anti-symmetrization of the two-body wave function, the shape of the correlation function can be related to the different emission time delay between the protons. This is formally stated in the *Koonin-Pratt* (KP) equation

$$1 + R_{\vec{p}}(\vec{q}) = 1 + \int S_{\vec{p}}(\vec{r}) \cdot K(\vec{q}, \vec{r}) \cdot d\vec{r} \tag{1.2}$$

where $1 + R_{\vec{p}}(\vec{q})$ is the two-proton correlation function, $S_{\vec{p}}(\vec{r})$ is the two-particles emitting source defined as the probability of emitting two protons

with a relative distance $\vec{r}$ measured at the time when the second particle is emitted, $K(\vec{q},\vec{r})$ is the kernel function and it contains the whole information about the final-state interaction between the two coincident protons, including their quantum statistics.
Since the correlation function is measured and the kernel function is well known for protons, solving equation 1.2 means extracting the source function, which retains the information on the space-time properties of the particle-emitting sources.
This can be achieved through different approaches, namely *Model Sources approaches*, *Shape-Analysis approaches and Transport Model approaches*. The first assumes a specific function underlying the shape of the correlation function. The second realeases such arbitrary assumption and numerically invert the equation. The *Imaging technique* is the most known and used method that belong to this group. The third compares the measured function to numerically computed models and allows probing transport properties such as nucleon-nucleon collision cross-section and the density dependence of the symmetry energy.
As an example, in Figure 1.2 (left panel) we show a set of proton-proton correlation functions, each of them corresponding to a different total momentum gating, for the reaction $^{14}N + {}^{197}Au$ at 75 MeV per nucleon. The dashed lines are computed assuming Gaussian-shaped source function. Figure 1.2 (right panel) shows the corresponding source functions computed with the imaging technique with no a priori assumption on the shape [7].

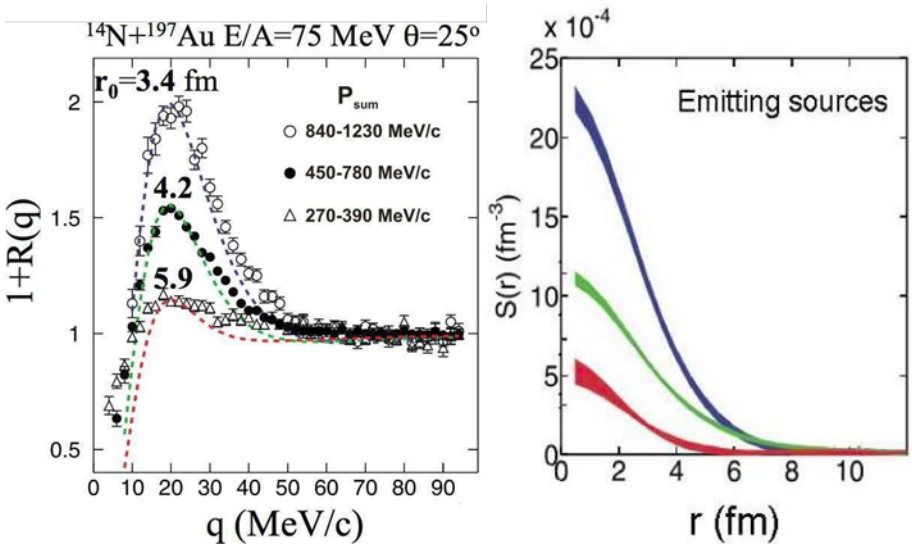

Figure 1.2: Example of proton-proton (left panel) correlation function for the reaction $^{14}N + {}^{197}Au$ at 75 MeV per nucleon. Each curve derives from a different total momentum gating. The dashed lines are computed assuming Gaussian-shaped source function. Right panel: corresponding source functions computed with the imaging techniques [7].

It is worth noticing that the order of magnitude of the spatial resolution is the fm. Since during heavy-ion collisions at intermediate energies a large variety of particles and fragments are produced, it is necessary to extend the application of the correlation function methods to the Light Charged Particles (LCP) and Intermediate Mass Fragment (IMF) other than protons. The complex scenario that emerges from these studies, consequence of the complex structure of LCPs and IMF, calls for higher-resolution detection systems in order to be properly addressed. Correlation functions with LCPs are at the basis of the emission time and chronology assessment for the particle-emitting sources, the understanding of which would facilitate the comprehension on primary fragments production mechanisms in heavy-ion collisions. IMF-IMF correlation functions are another important subject of study since they allow the extraction of the space-time properties of the nuclear system produced during the reaction at the time of their freeze-out stage. This gives a unique eye on multi-fragmentation phenomena and their

possible link to a liquid-gas phase transition in nuclear matter.
Two-nucleon correlation is also a precious tool to investigate the isospin dependence of the nuclear equation of state, which is perhaps the most uncertain property of neutron-rich matter.
The correlation function concept can be extended to a multi-particle scenario to explore the spectroscopic properties of the unbound states produced during the evolution of the nuclear system that follows the collision. This technique, called *Multi-Particle Correlation Spectroscopy* (MPCS), is a powerful tool since it allows disentangling simultaneous decays from sequential decays processes and gives access to characterization of the short-living exotic nuclei [7, 8].
Finally correlation measurements and the study of direct reactions in inverse kinematics with stable and radioactive ion beams (RIBs) push toward the measurements of momentum vector and of its correlation that imposes high energy and angular resolution. In addition two-or many-particle correlation measurements require large statistics that can be gained widening the solid angular coverage. The conflicting quest of performing correlation measurements of LCPs and IMFs or of joint detection of the emitted light particle and the residual heavy fragment arising from the stripping occurred in the incoming RIB in the study of direct reactions in inverse kinematics requires a wide dynamic range of the detector front-end electronics system. Moreover, the low energy foreseen for the RIB at SPES and SPIRAL2 requires low identification thresholds for both LCPs and IMFs, and the study of the correlation of LCPs even at high energies imposes a high stopping power. Last but not least, the geometry has to be as simple and versatile as possible to allow modular assembling and easy coupling with other detectors like spectrometers, neutron detectors and 4π arrays e. g. CHIMERA.

1.2 FARCOS project

The FARCOS (Femtoscope ARray for COrrelations and Spectroscopy) project is a detectors system with high pixelation capabilities in order to perform high precision measurements of two- and multi-particle correlations. It consists of a new array that is designed and constructed inside the INFN-

NEWCHIM experiment. The original idea, driving the construction of the prototype of FARCOS during the years 2010 – 2014 [9], has been developed inside of the CHIMERA/EXOCHIM collaboration with researchers and technical staff from the INFN-Sezione of Catania, Milano and Napoli, Laboratori Nazionali del Sud, University of Catania, Milano and Napoli, and including the participation of researchers from France, Spain and USA. An example of a configuration of FARCOS array is illustrated in Figure 1.3:

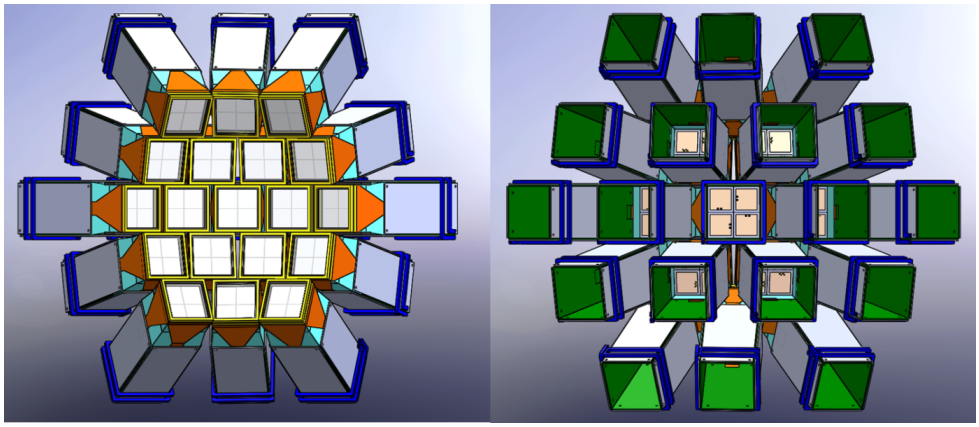

Figure 1.3: A possible configuration of FARCOS array, front view (left panel) and back view (right panel). Courtesy of C. Serrano and L. Acosta. For more details see chapter 2.

FARCOS will be a compact and relatively large-solid angle detection system, characterized by both high angular and energy resolution, modularity and having the peculiarity to be movable in a rather simple way in order to be coupled to different detector systems in laboratories around the world. In fact, it will be possible to use FARCOS not only coupled to CHIMERA detector [5], but also with others existing and under developing devices (as for example INDRA [10], GARFIELD [11], FAZIA [12], MUST2 [13]). Farcos must be designed to be able to cover different angular regions, depending on the physics case to be addressed, and on the beam energy and kinematics of the reaction. FARCOS array can be also used in coincidence with focal detection planes of magnetic spectrometers (as for example MAGNEX [14], PRISMA [15], VAMOS [16]). This can represent important progresses not only for typical studies on isospin physics, already covered in the framework

of the CHIMERA experiments [2], but also in studies of heavy-ion collisions, where two- and multi-particle correlations play a fundamental role in both dynamics and spectroscopy.
In summary, new perspectives will be opened in nuclear physics with both stable and radioactive beams working with the CHIMERA-FARCOS system at INFN-LNS, or coupling FARCOS with other detectors in national and international laboratories (as for example SPES - LNL, GANIL, GSI).
In particular, the FARCOS array is thought mainly to be used in the studies of correlations between charged particles in reactions at low and intermediate energies, as well as, in spectroscopic studies and in the raising investigations in the already mentioned femtoscopy studies, in order to extract information about the space-time properties of nuclear reactions. Recent advances in analysis techniques based on fitting or inversion procedures (as for example the imaging method) have allowed to get valuable information on the size (volume, density) of particle emitting sources produced during heavy-ion collisions, as well as their lifetimes [17]. Typically, these measurements are performed with devoted arrays of silicon and scintillator crystals covering a specific portion of the accessible phase space in the reaction. Then, the availability of powerful 4π detector, allows getting a unique tool to characterize the whole collision event in terms of impact parameter, reaction plane, collective motion and to extract important information about the dynamic and timescale of fragment emission [18].

1.3 Digital acquisition: advantages and disadvantages

Regarding the electronics for the FARCOS project, the first detector tests of the FARCOS prototype were performed by using the standard CHIMERA Front End electronics. In particular, due to the availability of the recent (2008) upgrading electronics for Silicon Pulse shape, we decided to use part of it. However because this electronics is too expensive, take too much space, need high power supply and consequently efficient cooling systems not always available, we decided to search for a new compact electronics

with good enough characteristics and reasonably low cost. After various test, the final choice was to design new ASIC preamplifiers for Silicon strips (developed at INFN and Politecnico of Milano), and to read and digitize the signals from such preamplifiers using the GET electronics recently designed for Time Projection Chamber (TPC) applications. Nevertheless, adapter boards must be developed in order to interface such ASIC preamplifiers with GET to match our needs of large dynamic range of the digital converters. CAEN(I)-Power supply are chosen for the bias of all the channels.
The foreseen number of channels for the FARCOS system when comprising 20 telescopes will be 2560 channels. This number of channels is large enough to discourage the use of SMD electronics of conventional SMD electronics. On the other hand, this number is too low to justify large efforts of dedicated man power for the development and adoption of a full VLSI readout electronics from the front-end to the back-end. In view of the main requirement of FARCOS, i.e., the flexibility and adaptability, especially due to the different envisaged physical cases, it is more reasonable taking into account for the available man power-expertise and budget constraints to develop a dedicated front-end while exploiting available solutions that can be customized thanks to the re-configurability offered by FPGAs systems for the back-end. Besides the already mentioned advantages, digital electronics allows us to obtain other ones. For example, an advantage of the digital acquisition is the fact that pedestal is measured event by event (by measuring the baseline of the preamplifier signal) and can be simply subtracted.
Moreover with digital acquisition the signal shape is completely saved/stored, allowing us to vary offline the parameters used in the software filters in order to improve resolution and ratio of signal/noise.
Obviously we have to pay a price for all such advantages. In this case, the price is that one need a very large disk storage space available in order to save the complete trace of the signals. Moreover, the transmission bandwidth of ACQ system must be very large to be able to transfer from the readout electronics to the storage farm the full amount of data to be processed. Finally yet importantly, we need a very large CPU-power for the on-line and off-line computer farms in order to check the progress of the experiment and to do the complete data analysis. These aspects will be better analyzed in

the following.

1.4 Software filters

Digital FIR (Finite Impulse Response) filters are applied in our signal processing analysis to the signals after baseline restorer. The way to obtain a digital filter is to define a convolution of the input signal s_j with the digital filters "response function" r_k of finite duration M:

$$(r * s)_j = \sum_{k=-\frac{M}{2}+1}^{\frac{M}{2}} s_{j-k} r_k \tag{1.3}$$

The digital filter is called finite when the response function is different from zero in the interval $-\frac{M}{2} < k \leq \frac{M}{2}$ and zero otherwise, where M is an even integer number. When the impulse response is used in this way it is also called "filter kernel" because can be easily pre-calculated for a given response function in a window with a number of discrete points equal to M (we shall define in the following the number of samples M as number of "taps").
In our signal processing for the GET acquisition we have mostly often used the so-called "triangular filter" (see Figure 1.4) [19].

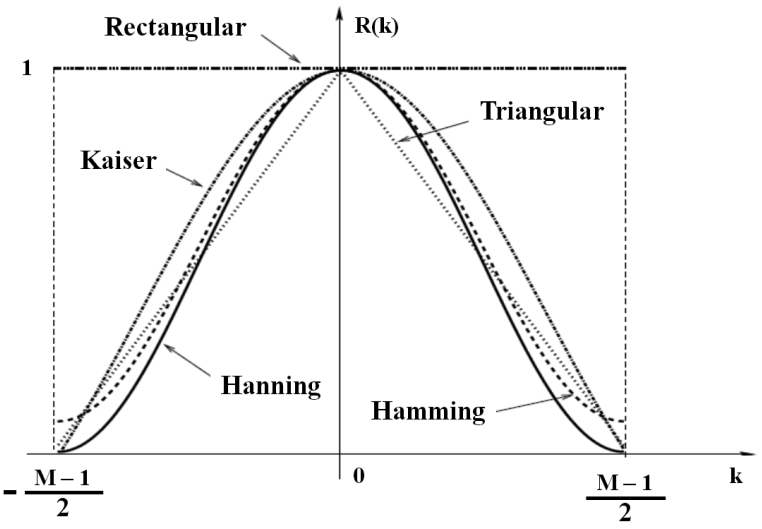

Figure 1.4: Response function that we used (Triangular filter) in comparison with other kind of filters (Kaiser, Rectangular, Hanning and Hamming).

The response function $R(k)$ is approximated, using a symmetric triangle, in a window defined as:

$$R(k) = \begin{cases} 1 + \frac{2k}{M} & \text{if } -\frac{\mathrm{M}-1}{2} \leq \mathrm{k} < 0 \\ 1 - \frac{2k}{M} & \text{if } 0 \leq \mathrm{k} \leq \frac{\mathrm{M}-1}{2} \end{cases} .$$

The number of M points used is strictly dependent from the kind of calculation we want to perform on the original signal. For example, in the calculation of a rise-time, filters with a low number of taps are used (or no filter at all) in order to avoid signal distorsions, while filters with a big number of taps are more suitable for the evaluation of the signal maximum amplitude.
In Figure 1.5 we show the results of application of the triangular filter to determine the rise-time (blue lines with 17 taps used) and the signal amplitude (green lines with 251 taps used) for digitalized waveforms of a Silicon detector and of a CsI(Tl) scintillator (red lines).

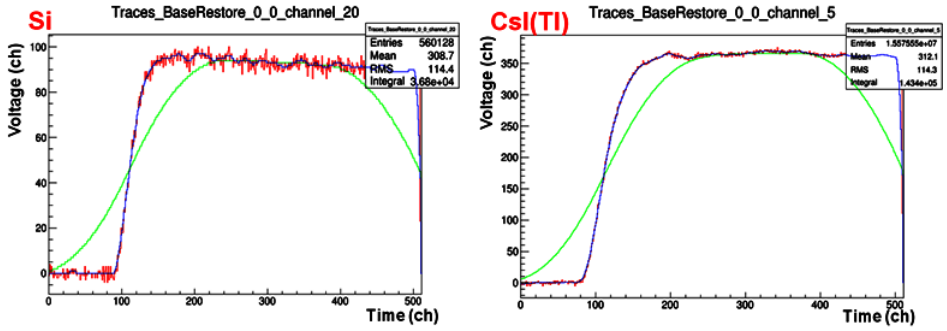

Figure 1.5: Digitized waveforms (red lines in both panels) of a Silicon detector (left panel) and of a SI(Tl) scintillator (right panel), digitally filtered signals used to determine the signal amplitude (green lines in both panels) and filtered signals used to determinate the rise-time (blue lines in both panels).

As shown in Figure 1.5, using triangular filters is a good compromise because we obtain good results saving, at same time, the CPU machine time in the online analysis because the calculation is relatively fast (depending on the number of the filter taps).

Chapter 2

Experimental set-up

2.1 CHIMERA

CHIMERA (Charged Heavy Ion Mass and Energy Resolving Array) is a 4π multi-detector designed to study heavy-ion collisions in the intermediate and low Energy range. It can be schematically described as a set of 1192 detection cells arranged in 35 rings following a cylindrical geometry along the beam axis. The whole apparatus has a total length of about $4\,m$, as illustrated in Figure 2.1, and it is setup in a vacuum chamber.

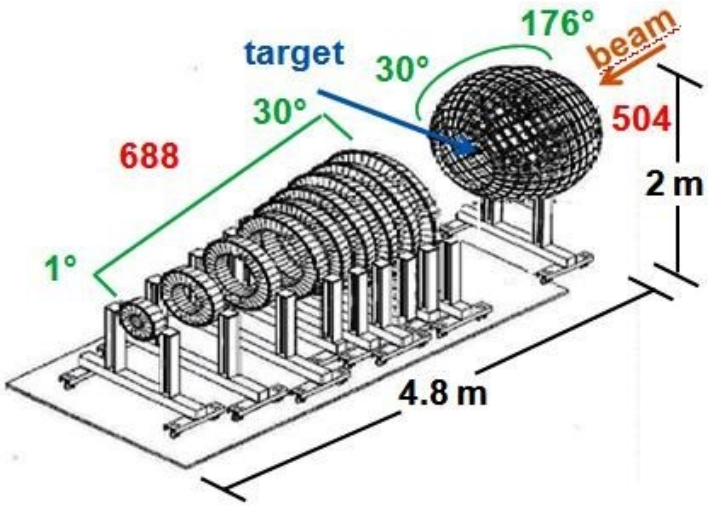

Figure 2.1: Schematic representation of CHIMERA apparatus.

The basic detection module of CHIMERA is a telescope made of a Silicon detector (Si), followed by a Cesium Iodide Thallium activated scintillation detector (CsI(Tl)), coupled to a photodiode Figure 2.2.

Figure 2.2: The basic detection module of CHIMERA apparatus.

The mechanical structure can be essentially divided into two differently shaped blocks: the forward one (see Figure 2.3), covering the polar angles between 1° and 30°, is made of 688 modules assembled in 18 rings, grouped in couples, and supported by 9 wheels centered on the beam axis. The rings of telescopes are placed at a distance from the target varying from 350 to 100 cm, with increasing polar angle. Each wheel is divided into 16, 24, 32, 40 or 48 trapezoidal cells, depending on its polar coordinate, containing each one a detection module, or telescope.

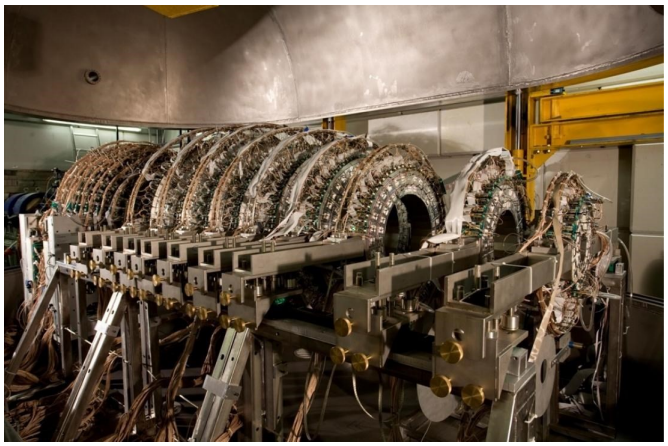

Figure 2.3: Photo of the nine wheels of the CHIMERA multi-detector.

The remaining angular range, between 30° and 176°, is instead covered by the sphere of 40 *cm* internal radius (see Figure 2.4).

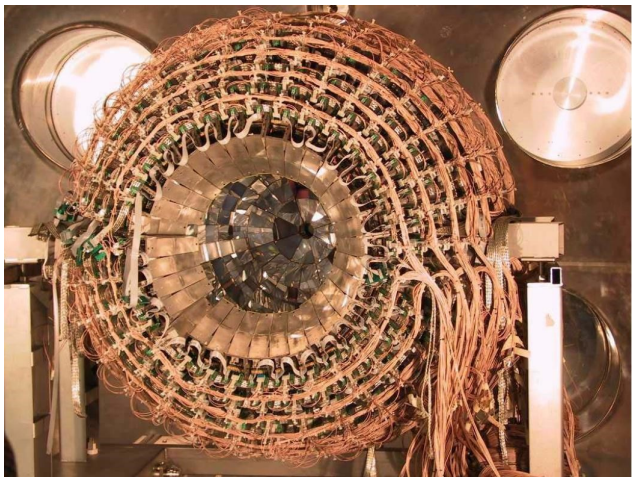

Figure 2.4: Photo of the sphere of the CHIMERA multi-detector.

Whose 15 forward (according to the beam direction) rings are segmented into 32 cells while the two most backward ones are segmented into 16 and 8 cells respectively. Each module of this spherical structure consists in a steel box containing the Cesium Iodide crystal with the Silicon detector placed at its front end. The large number of telescopes and the geometrical configuration give to CHIMERA a high granularity, thus reducing the multi-hit probability, and a high solid angle coverage, about 94 % of 4π. All these features, in addiction to low energy detection threshold, give the possibility to have a complete event reconstruction.

RING	Dist.[cm]	$\theta_{min}[^o]$	$\theta_{max}[^o]$	$\Delta\phi[^o]$
1	350	1.0	1.8	22.50
2	350	1.8	2.6	22.50
3	300	2.6	3.6	15.00
4	300	3.6	4.6	15.00
5	250	4.6	5.8	11.25
6	250	5.8	7.0	11.25
7	210	7.0	8.5	9.00
8	210	8.5	10.0	9.00
9	180	10.0	11.5	9.00
10	180	11.5	13.0	9.00
11	160	13.0	14.5	7.50
12	160	14.5	16.0	7.50
13	140	16.0	18.0	7.50
14	140	18.0	20.0	7.50
15	120	20.0	22.0	7.50
16	120	22.0	24.0	7.50
17	100	24.0	27.0	7.50
18	100	27.0	30.0	7.50
19	40	30.0	38.0	11.25
20	40	38.0	46.0	11.25
21	40	46.0	54.0	11.25
22	40	54.0	62.0	11.25
23	40	62.0	70.0	11.25
24	40	70.0	78.0	11.25
25	40	78.0	86.0	11.25
26	40	86.0	94.0	11.25
27	40	94.0	102.0	11.25
28	40	102.0	110.0	11.25
29	40	110.0	118.0	11.25
30	40	118.0	126.0	11.25
31	40	126.0	134.0	11.25
32	40	134.0	142.0	11.25
33	40	142.0	150.0	11.25
34	40	150.0	163.0	22.50
35	40	163.0	176.0	45.00

Figure 2.5: Geometrical characteristics of the CHIMERA array. For each detector in a ring, the distance from target, minimum and maximum polar angle, azimuthal angle range and covered solid angle are specified.

2.1.1 Basic detection module

Each module of CHIMERA is composed by two-detection stage: the first one is a $300\,\mu m$ thick Silicon detector. As well known, Silicon is a very widely used material for particle detectors, because of its good energy resolution, its high density ($2.33\,g/cm^3$), the low energy needed to create an electron-hole pair ($3.6\,eV$ with respect to $30\,eV$ in gases), its fast signal collection (about $10\,ns$ in $300\,\mu m$ of thickness for light particles) and its good time resolution. In particular, the Silicon detectors used in CHIMERA have a trapezoidal shape and were made by using the planar technology [20]. With this technique, it is possible to have well defined detector thickness, very sharp active zones (the $p+$ layer inactive area is 500 $\mathring{A}$ thick), and extremely thin and homogeneous junction thickness. These Silicon detectors have a geometry that changes according to the position in the device. In the forward part of the apparatus, each cell contains two telescopes, and thus two Silicon detectors (internal and external detectors in the same pad) characterized by the presence of two active zones that work independently of one another.
Both the active zones are surrounded by a guard ring located $50\,\mu m$ away in the dead zone (due to the planar technology) of the edge of the detector. The 504 Si detectors of the sphere instead are simple pad detectors; even in this case a $500\,\mu m$ dead zone, in which a guard ring is placed, surrounds the active area. A schematic representation of wheels and sphere Silicon detector is shown in Figure 2.6:

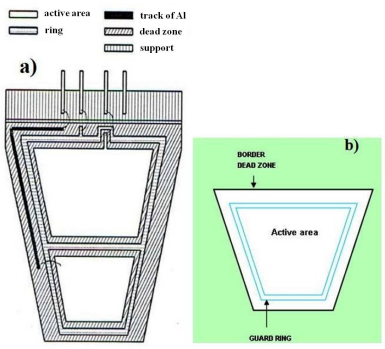

Figure 2.6: A schematic view of wheels (a) and sphere (b) Silicon detector.

The second stage of CHIMERA's telescope consists of Cesium Iodide Thallium activated crystals CsI(Tl); these scintillators are used to measure the residual energy of particles that punch through the Silicon detector [21]. This kind of crystals are chosen as second stage detectors because of their high density, so that their high stopping power allows to reduce the thickness needed to stop high energy charged particles and fragments. Moreover CsI(Tl) scintillators are characterized by relatively low cost, simple handling, a good resistance to radiation damage and external factors, good light output performance when coupled with a photodiode or a photomultiplier, and offer the possibility to make an isotopic identification. In fact the light versus time shape of the output signal from the scintillator, consist of a fast component and a slow one whose decay constants depend on the specific energy loss of incident fragments, and therefore on their energy, charge and mass [22]. A disadvantage of these scintillators is the non-linearity (at low energies) in light response that is therefore not directly proportional to deposited energy, depending on the nuclear species of the fragment and on its ionizing power. The shape of CHIMERA's crystals is a truncated pyramid with a trapezoidal base; the dimensions of the front surfaces are the same of the Silicon detectors and depend on the position in the device. The backward surface is bigger than the front one, depending on the thickness of the crystal that ranges from 3 to 12 cm.
Finally, the CsI(Tl) crystals are coupled with photodiodes (PD), preferred to photomultipliers mostly for their low operating voltage (so low power dissipation), their simple handling and compact assembly under vacuum. The used photodiodes, manufactured by Hamamatsu Photonics, are 300 μm thick with an active surface of $18 \times 18\, mm^2$ and are located into a ceramic support with the front side (corresponding to the light entrance hole) protected by a thin window of transparent epoxy resin.

2.2 Electronic chain

Two different electronic chains handle the signals coming from Silicon detectors and photodiodes; these chains process and digitize signals read by the acquisition system. In a typical experiment performed by means of

CHIMERA apparatus it is necessary that electronics satisfy some requirements such as a large dynamic range (from MeV to GeV), a low power dissipation under vacuum, a good timing in order to reach a resolution of about 1 % in velocity measurements through the TOF technique [23], a good energy resolution and high level of flexibility in coupling the detector with other experimental devices. With the aim to reduce electronic noise and signal losses in parasitic circuits, which strongly affect the energy resolution, the preamplifiers (PA) of Silicon detectors and photodiodes are placed on a motherboard inside the vacuum chamber. The motherboards for the detectors of the forward part are located on the external surface of the wheels and contain four PAs: two for the internal telescope and two for the external one, since each telescope needs two PAs, one for the Silicon detector and the other for the photodiode. On the other hand, the motherboards in the sphere have only two preamplifiers, corresponding to only one telescope, and they are located on the top of the metallic baskets containing telescopes. All the motherboards are cooled for stability of the electronics. The voltage generators for detectors and preamplifiers with the rest of electronic chain are placed outside the vacuum chamber.

2.2.1 The electronic chain of Silicon detectors

The recently upgraded basic electronic chain of Silicon detectors is shown in Figure 2.7:

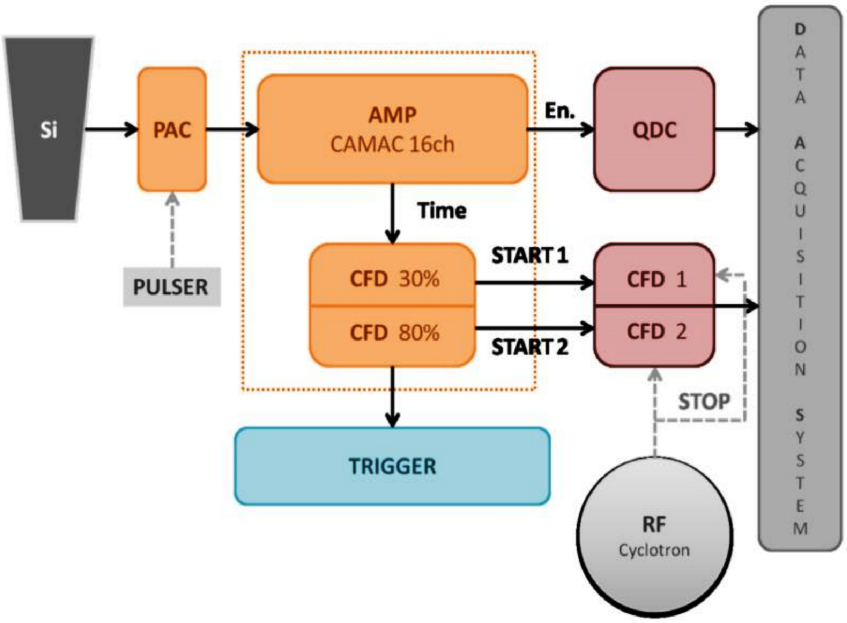

Figure 2.7: The basic front-end electronics of Silicon detectors.

A charge preamplifier (designed to reach good timing measurements with high capacitance detector) provides a first amplification of signals; it integrates the signal of the detector giving an output independent of detector capacity and proportional to the charge produced by detected particles. In order to control electronic stability, each preamplifier is provided with a test input, which accepts signals coming from a pulse generator. The output is a single negative fast signal carrying time and energy information, characterized by a rise-time from 10 to 200 ns and a decay time of about 200 μs. The preamplifier sensitivity changes with the polar angle: in the most forward part ($\theta = 1° \div 10°$), where the more energetic particles are expected, the sensitivity is 2 mV/MeV, while at larger angles ($\theta = 10° \div 176°$) it is 4.5 mV/MeV. Then the output signal is processed by the amplifiers (pulse shape) channels model N1568, produced by CAEN. Such compact modules are particularly studied to measure the rise-time of the Silicon signal, enabling us to get the charge of particles stopped in the first detection stage [24]. In order to measure the rise-time of Silicon signals, each channel is equipped with two different discriminators, characterized by different constant fraction (30 % and 80 %). These two CFDs process two copies of the same timing signal

and send their output signals to two different TDCs; each TDC, working in common stop mode, measure the time from the start signal given by the pulse shape module, and the stop signal generated using the cyclotron phase. The time measured by the $T_{30\,\%}$ channel is used for time of flight evaluation, while the difference between $T_{30\,\%}$ and $T_{80\,\%}$ TDCs is used to evaluate the signal rise-time.
The pulse shape module is also equipped with a stretcher that prepare the energy signal to be integrated in a simple way by a Charge-to-Digital Converter (QDC). The QDC is able to perform a double charge encoding: the High Gain (HG) and the Low Gain (LG) coding. In the first case, an amplification factor $8\times$ is applied in order to obtain a good energy resolution also for low Energy signals. The module can also produce a chainable multiplicity signal. This signal has a level of $25\,mV$ for each fired channel in the chain, and it is used for the event trigger.
Detailed information about general architecture of CHIMERA Data Acquisition System can be found in [25]-[30].

2.2.2 The electronic chain of CsI(Tl) crystals

The old electronics for the CsI line is going to be replaced because it is based on amplifiers SILENA not more in production since more than 10 years. We will not discuss the details of such old electronics because it will be replaced by the GET one. In the GET chapter some examples will be given of the different results obtained using the two electronics. Only the preamplifier under vacuum will be maintained. The signal coming from the CsI(Tl) (coupled with a photodiode) detector firstly is processed by a charge preamplifier that presents the same characteristics of those used for Si detectors, except for the sensitivity that is of the order of $50 \div 100\,mV/MeV$. The rise-time of output signals is significantly longer than $50\ ns$ because of the scintillation light characteristics.

2.3 FARCOS

The following paragraphs are devoted to describe the FARCOS (Femtoscope ARray for COrrelations and Spectroscopy) project, aimed at the

development of a detection system with high pixelation capabilities in order to perform high precision measurements.

2.3.1 Main characteristics of the FARCOS array

FARCOS has been conceived as a compact high resolution array; the basic telescope consists of two DSSD (Double-sided Silicon Strip Detector) 300 μm thick and 1500 μm thick, as first and second stage respectively. The third stage is constituted by 4 CsI(Tl) crystals; each of them has a length of 60 mm and a sensitive area of $32 \times 32\, mm^2$, arranged in square configuration 2×2. Each crystal produces a scintillation light collected by Silicon photodiodes 300 μm thick with an area of $18 \times 18\, mm^2$. The total detection area of Silicon detectors is $64 \times 64\, mm^2$, adapted to cover the total area of the four CsI(Tl) crystals placed behind. The scheme of the three stages of one FARCOS cluster is shown in Figure 2.8:

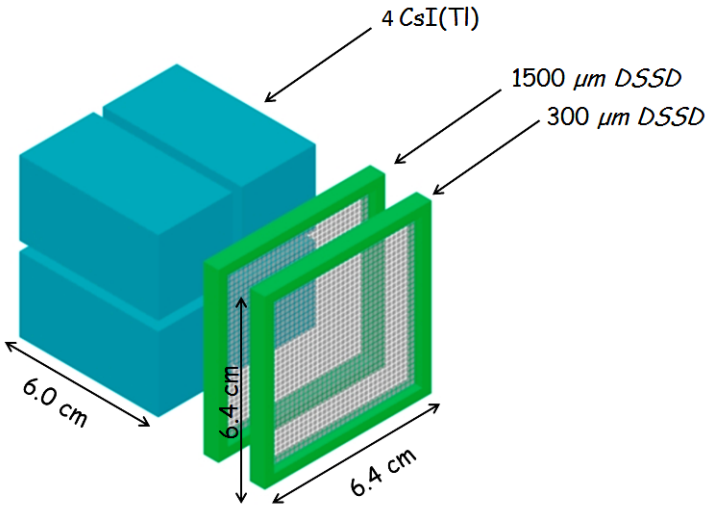

Figure 2.8: Schematic representation of a FARCOS module.

Each DSSD features 32 horizontal and 32 vertical strips providing 1024 equivalent pixels of $2 \times 2\, mm^2$. This segmentation allows to reconstruct the impact position of detected particles, hence their emission angles, with high resolution. High angular resolution combined with high energy resolution provide a good measurement of relative energy and momentum vector. The

performance of FARCOS allows one to detect particles in a wide dynamic range going from MeV to GeV; the high stopping power of thick CsI(Tl) allows indeed to stop high energy light particles, while low thresholds for particle identification will be attained with pulse shape techniques applied to the first DSSD [31].

2.3.2 Detector: the CsI(Tl) stage

The final configuration of the FARCOS CsI(Tl) detector is a truncated pyramidal shape with the square basis of the backward face (where photodiode is mounted) of the order of $38 \times 38\, mm^2$ and a front face of $32 \times 32\, mm^2$. This shape ensures that particles impinging on the second and 31^{st} strip of the second stage Silicon detector are correctly stopped inside the CsI(Tl). While particles impinging on the first and 32^{nd} strips can escape from CsI(tl) before being completely stopped when the telescope is placed at a distance of $25\, cm$ (distance of the second Silicon stage) from the target. This choice moreover was performed in order to limit the size of telescopes, allowing a more compact mounting if different detection distance are needed. On the other hand, because of the finite size of Silicon strips, some typical known problems arise for the good definition of the effective solid angle of the first and last strips in matching the two silicon stages. However, the more external strips generally suffer of a larger noise (with respect to the internal ones) and are often excluded from the analysis, so, it is very important to save data coming from the second and 31^{st} strips. This truncated pyramidal shape has also the advantage to allow a more sure mounting of CsI(Tl). With this shape in fact, the crystal cannot be pushed from the back (wedge effect), so saving for accidental touches of the bonding of the back side of Silicon strip detector. Obviously this means that the global size of telescopes (taking into account also electronic boards) will be larger than the one of Silicon strips (including package the side of front surface becomes $72\, mm$) and it will produce a slightly smaller efficiency in the coverage of solid angle, more important when detector will be mounted far from the target. Nevertheless this is a relatively good compromise between the solid angle coverage and detector performances.

2.3.3 Positioning system of FARCOS telescopes

In order to perform high precision measurements of two- and multi-particle correlations it is necessary to determine with high accuracy the absolute angular position of every pixel with respect to the beam line.
The system we have developed is based on a laser source placed at 0°, 5 m after the target position for mounting inside the CHIMERA chamber.
The laser beam, characterized by a diameter of 0.8 mm and a divergence of 1.0 $mrad$, will be directed on a mirror placed in the target position, and reflected towards the detector, as shown in Figure 2.9:

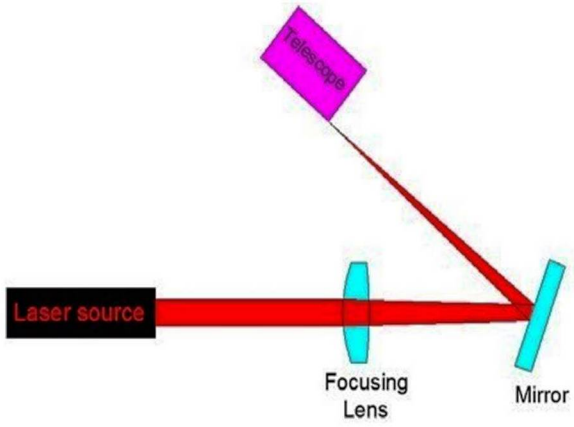

Figure 2.9: Outline of the laser beamline designed for the exact positioning of every telescope.

The laser beam moreover will be pulsed in short bunches, in order to produce a detectable signal on the fired strip of the first DSSD. The mirror will be mounted on a scanning Galvo system [32] (see Figure 2.10) which will rotate it around a horizontal axis with angular resolution of 0.01°.

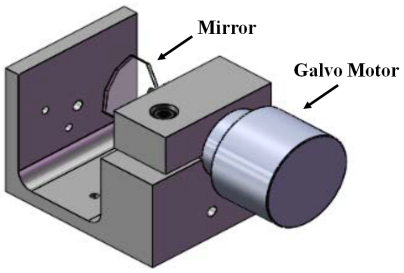

Figure 2.10: Galvo system used to rotate the mirror placed in the position of the target.

The Galvo system will be installed on the target support, which will rotate the galvo system around the vertical axis with angular resolution of 0.01°. After a suitable calibration this system can ensure the positioning of telescopes with adequate precision; the main error we could make is produced by a displacement of the mirror located in the target position. Using a converging lens placed before the mirror, laser beam will be focused on several reference points chosen on every telescope.

Figure 2.11: Reflecting system of the laser beam positioned in CHIMERA vacuum chamber during various tests at LNS.

2.4 GET electronics

In the last decade the development of more and more powerful digital devices, the availability of fast relatively low cost storage devices, and the improvement of data transmission speed, due to optic fiber technology, allowed the development of new fully digital data acquisition systems. As already mentioned, in such data acquisitions the complete shape of the signal can be stored. This is a big advantage because the signal treatment can be changed and adapted to any different experimental condition. Sophisticated software filter can be applied to clean signal from noise. The pedestal can be measured event by event, largely improving resolution. Pulse shape analysis of the detector signal can be applied, improving particle identification capabilities, but also allowing to clean pile up events. Last, but not least, very sophisticated filter can also be optimized to extract more precise timing information. One of the last developed ACQ SYSTEM of such kind is the GET one. This electronics was developed, in the last years, with the aim to produce a low cost and very flexible electronics for the new generation of TPC under construction in the world. Many laboratories joined their efforts to build such new electronics (Saclay, Ganil, Bordeaux, MSU, RIKEN), and nowadays it is adopted or tested by more than 20 new detector system in constructions around the world. The flexibility of such electronics was fully shown by the fact that many detector system that now are going to use it are different than TPC.
GET eletronics is based on AGET asic chip [33] (Asic for General Electronics for Tpc) circuit (see Figure 2.12) produced by CEA laboratory at Saclay.

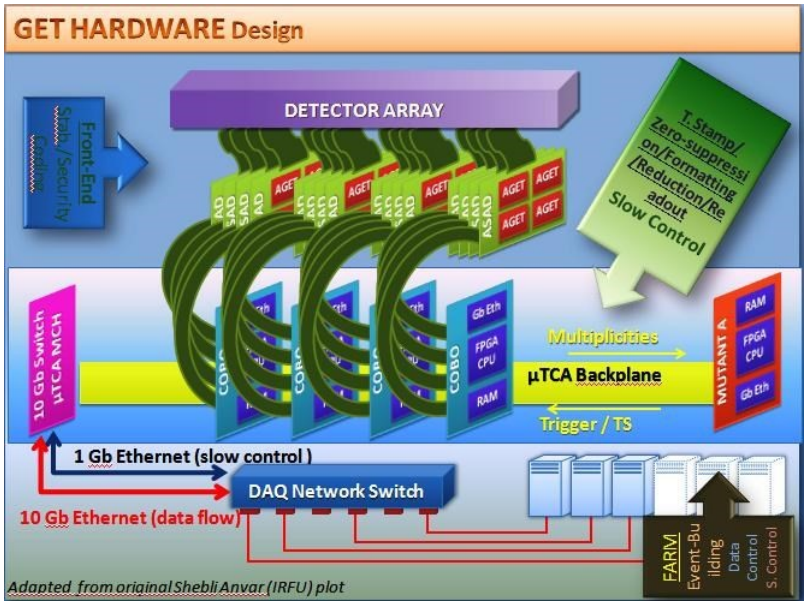

Figure 2.12: Schematic representation of GET electronics.

Four of these chips are soldered on the ASAD (Asic Support and Analog-Digital conversion) card with four 12-bit ADC (one per AGET). Each AGET handles up to 64 channels (256 inputs for ASAD). The digital outputs of the 4 ADCs are transmitted with a maximum speed of $1.2\,Gbit/s$ to the CoBo board. The CoBo (Concentration Board) manages up to 4 ASAD, so using 4 CoBo we are able to manage more than 4000 detectors. The CoBo board is responsible for applying a time stamp, zero suppression and compression algorithms to the data. It will also serve as a communication intermediary between the Asad and the outside world with a maximum speed of $1\,Gbit/s$ per CoBo. The MUTANT (MUltiplicity Trigger ANd Time) card manages the multiplicity, conditions for the trigger, and the distribution of the clock on the whole system. It also allows conversation with other acquisition systems by transferring/receiving external triggers. The global data are transmitted through network switch to a computer farm with a maximum speed of $10\,Gbit/s$ for storage and online analysis.
The CoBos and the trigger (MUTANT) modules are housed in a µTCA (Micro Communications Computing Architecture) crate that can host up to 11 CoBos and 1 trigger module. It implements a serial backplane bus and

a network Ethernet infractructure built into the system. We have adopted the Vadatech VT893 µTCA crate [34] that is already validated to operate with the GET electronics. Through the TCA Ethernet switch the CoBo(s) can exchange data up to $10\,Gb/s$ with an external computers farm for data analysis and storage.

The main characteristics of GET electronics is flexibility and programmability of the system. One can easily change gain, adjust the time scale to cope with timing of the detector, adapt the trigger system not only using the information on channel multiplicity but also on the position of fired channel. A single channel in its standard version integrates mainly: a charge sensitive preamplifier, an analogue filter (shaper), a discriminator for trigger building and a 512-sample analog memory (SCA) (see Figure 2.13).

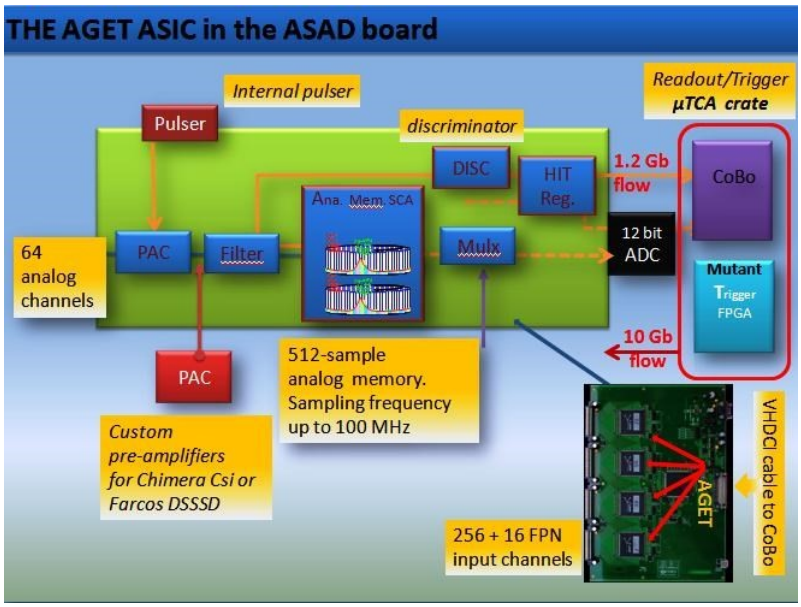

Figure 2.13: Scheme of a single channel of the AGET chip.

The analog filter is formed by Pole Zero Cancellation stage followed by a 2-complex pole Sallen-Key low pass filter. The peaking time of the global filter is selectable among several values (16 values) in the range of 70 ns to $1\,\mu s$. The filtered signal is sent to the analogic memory and discriminator inputs.

The memory is based on a Switched Capacitor Array structure (SCA). A

512 cell-depth circular buffer is used, in which the analogic signal coming out from the shaper is continuously sampled and stored. The sampling frequency can be set from 1 *MHz* to 100 *MHz*. The sampler is stopped on a trigger decision. In the read out phase, the analogue data are multiplexed in time domain toward a single output and sent to the external 12-bit ADC at the readout frequency range of 25 *MHz* . In the nominal mode, the input signal goes through the input of the CSA (Charge Sensitive Amplifier). By slow control, it is possible to switch the signal to the input of SKfilter or inverting 2× Gain just before the SCA. In this case, the internal supply of the CSA and PZC filter is cut off.

Part of the SCA noise will be probably coherent between channels; to perform common mode noise rejection, 4 extra channels named FPN (Fixed Pattern Noise) are included in the chip. FPN channels are treated by the SCA exactly as the other channels. Offline, their outputs can be subtracted to the 64 analog channels. This pseudo-differential operation is supposed to reject the major part of the coherent noise due to 2× Gain of Gain2 and SCA such as clock feed-through and couplings through the substrate. It also improves the power supplies rejection ratio (PSRR) of the chip.

These channels are distributed uniformly in the chip and their readout indexes are: 11, 22, 45 and 56. To reduce the amount of data and dead time, we decided to enable only a FPN (channel 11) for each AGET subtracting it to the other 64 analog channels. As already mentioned a FARCOS telescope is constituted by 2 DSSD 32×32 strips and 4 CsI(Tl) detectors with photodiode readout. To save electronics it was decided to use back strips only for one DSSD (the first or the second stage depending on physics case). Moreover, double dynamics is fundamental in the case of front strips while it is less important for the back side that is not characterized by very good resolution. So we need two electronic channels for each front strip and only 32 channels for the back strips. The double dynamics is also necessary for the CsI(Tl), therefore we need 8 more electronic channels for each telescope. In summary for each telescope we need 128 electronic channels for the front strips, 32 channels for the back strips and 8 for the CsI(Tl). For the 20 telescopes we therefore need 10 ASAD cards for front strips, 3 ASAD cards for the back strips (one half filled), and 1 ASAD card for CsI(Tl) (with only 160

channels filled). We cannot mix back strips electronics and CsI(Tl) because they need a different treatment of signals. 100 *MHz* sampling frequency is in fact required for silicon signals while 50 or probably better 25 *MHz* is required for CsI(Tl) signals.
We will not use the preamplifier input of AGET chips. During the tests we have seen that one can very well use either the SKfilter input, if the signals had some noisy in order to improve resolution or directly the Gain2 input when this is not necessary. Depending on the physics case, one has also to take into account that in SKfilter mode one has a factor $\times 2$ gain; therefore, the maximum energy of the allowed dynamic range is consequently reduced. GET electronics will be used for the CsI(Tl) of CHIMERA and for all FARCOS.
To read 14 ASAD cards one needs at least 4 CoBo cards. Notice that by using more CoBo cards it is possible to reduce the total dead time; in fact by reducing the number of channel read through each CoBo, one will have a larger band width for each channel in the transfer trough Ethernet to the PC farm dedicated to the on-line analysis and data storage.
One MUTANT board is clearly required to manage the trigger, the synchronization of all CoBo cards among them and of the GET ACQ with the other ACQs needed for the detector systems to be coupled to FARCOS.

2.5 The Dual Gain Module

As described in previous paragraph, for some of the channels of FARCOS and for CHIMERA CsI we need to implement Double dynamical range. We therefore had to develop some adapter cards, slightly different for CHIMERA and FARCOS that will do:

1. the conversion from differential to single-ended signaling (only for FARCOS);

2. the splitting of signals for the case of detector front strip for FARCOS and for CHIMERA CsI;

3. independent gain adjustment for the two series of splitted signals, with possibility to have selectable gains $\frac{1}{8}$, $\frac{1}{4}$, $\frac{1}{2}$, 1, 2, 4, 8;

4. signal level adapter (AGET chips works better if signals have a positive baseline from 0.5 to 2 V).

We need therefore to develop three different interface cards. A DUAL gain module for FARCOS (with differential input) a DUAL GAIN for CHIMERA (with single ended input) and single gain with level adapter for back strip of FARCOS. Because the philosophy of the different cards is similar we will describe here the dual gain module for CHIMERA.
The Dual Gain Module is a multichannel digitally programmable gain amplifier (PGA). The module split each FARCOS/CHIMERA channel and adjust the signals level to the ASAD input dynamic range. The Dual Gain Module will be developed with a form-factor as the one used for the ASAD board (VME) in order to optimize the connection between the two boards. In this configuration, each ASAD card will be connected to two Dual Gain Modules. The detail of the set-up is shown in Figure 2.14:

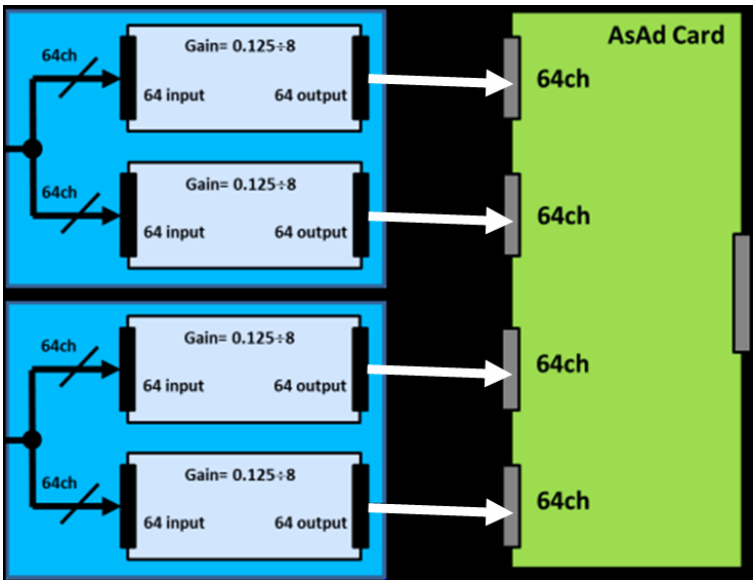

Figure 2.14: ASAD card and Dual Gain Module connection diagram.

To prevent the output signal from swinging outside the common-mode input range of the ASAD card each PGA channel provides both high and low output clamp protection. In addition, the PGA allows the output signal baseline setup. The Dual Gain Module is based on a microcontrollers system

that will take care of the module slow-control, the parameters setting and the user communication through a dedicated communication bus.
The electronics consumer device used to amplify or attenuate the signal consists of a separate low-noise input preamplifier and a programmable gain amplifier. To evaluate and test the PGA performances some beta-cards were developed and results of the test are described later in this work.
The input impedance of every channel is $50\,\Omega$ while the output impedance can be $50\,\Omega$ for long cable transmission systems or high impedance ($10\ K\Omega$ typically) for short cable. The user can digitally set the gain in the range from $0.032\,V/V$ to $4\,V/V$ (from $-30\,dB$ to $12\,dB$) at $50\ \Omega$ output impedance. Moreover one can double the gain range using high impedance load.

2.6 Identification techniques

During our tests on GET electronics we have used various methods to identify particles in charge and/or mass. In this paragraph we will give some generalities about the used identification techniques. More details will be given in next chapters with many examples. The energy measurement is based on the physical process by which a charged particle loses part of its (or the whole) energy when crosses a material. The identification methods until now adopted are three:

1. ΔE-E *technique*, using the signals coming from the Silicon and the CsI(Tl) detectors, is employed for charge identification of heavier ions, and charge and mass identification of the lighter ones;

2. *E-RiseTime*, obtained by signals coming out from the CsI(Tl) detectors. Test were also performed with silicon signals;

3. *Pulse shape discrimination technique*, using the fast and slow component of signals, can be also used to identify the light charged particles; this method was used with the previous CsI(Tl) electronics allowing isotopic separation for energetic particles with $Z \leq 4$ stopped in the CsI(Tl) scintillator. It can be also used with GET as was shown in previous test with other digital acquisitions [35].

The effective identification limits depend on atomic number, mass and energy of detected particle, and on the position of the detector.

2.6.1 ΔE-E technique

Thanks to the use of telescopes constituted by combination of two or more detectors, it is possible to identify in charge and mass the particles through the ΔE-E technique. Due to inelastic collisions with atomic electrons and ionization of the target nuclei, a charged particle that crosses a material layer loses energy. The average energy lost per unit path, called "stopping power" (indicated by the symbol $\frac{dE}{dx}$) depends on charge, mass and energy of the incident particle, according to the following approximation of the Bethe-Block formula:

$$\frac{dE}{dx} \propto \frac{AZ^2}{E} \tag{2.1}$$

where A, Z and E correspond to the atomic mass number, the atomic number and the kinetic energy of the incident particle respectively. If the particle, in our case the reaction fragment, is energetic enough to punch through the Silicon detector with thickness, and if the detector response goes linearly with the deposited energy, the output signal has an amplitude proportional to:

$$dE \propto \frac{dE}{dx}\Delta x \tag{2.2}$$

then, if the incident particle is stopped in the scintillator, the output fast component signal from this last stage of the telescope is proportional to residual energy just released in Cesium, E_{res}. The sum of these quantities gives the total kinetic energy of the particle:

$$E = \Delta E_{si} + E_{res(CsI)} \tag{2.3}$$

combining the two quantities in equation 2.2 and equation 2.3 several groups of hyperbole's branches are noticeable in a ΔE-E scatter plot: each group corresponds to a Z value and, inside it, each branch corresponds to a different isotope of the same element. Often however ΔE-$E_{res(CsI)}$ are also used for such identification bidimensional histogram neglecting ΔE_{si} in equation 2.3 (see Figure 2.15).

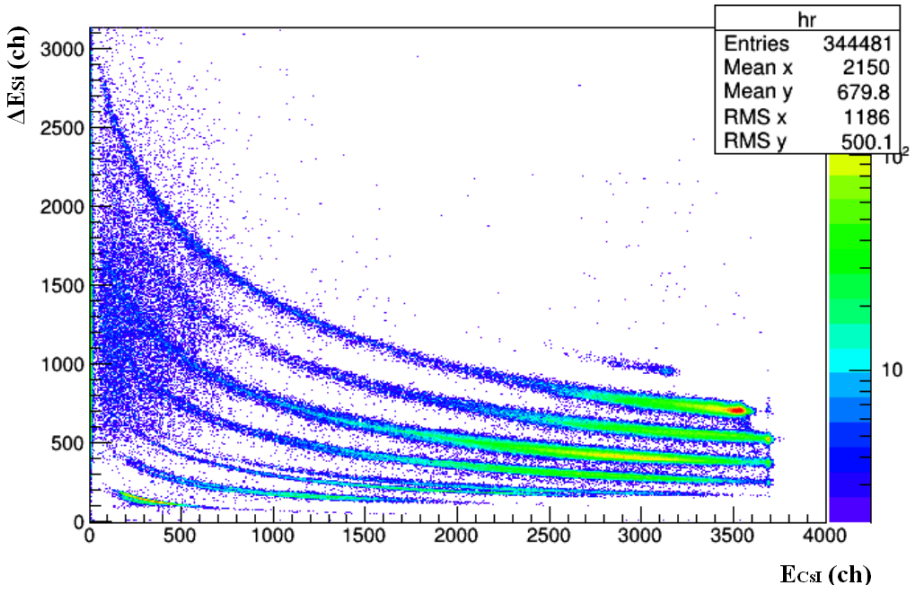

Figure 2.15: Bidimensional histogram obtained with ^{16}O beam at 55 $AMeV$ and using GET electronics, isotopic resolution can be seen for Be ions.

2.6.2 E-RiseTime technique

This technique consists in determining the rise-time (from 20 % to 80 %) for the digital signal. This is done using a software triangular filter (which we will discuss in the next chapter) with a given number of taps (the number of nodes can be changed off-line to improve the identification of the detected particles in CsI(Tl) scintillators). A rise-time analysis was performed with quite good results as shown in Figure 2.16. As for the ΔE-E method, also in this case each group corresponds to a Z value and, inside it, each branch corresponds to a different isotope of the same element (see Figure 2.16).

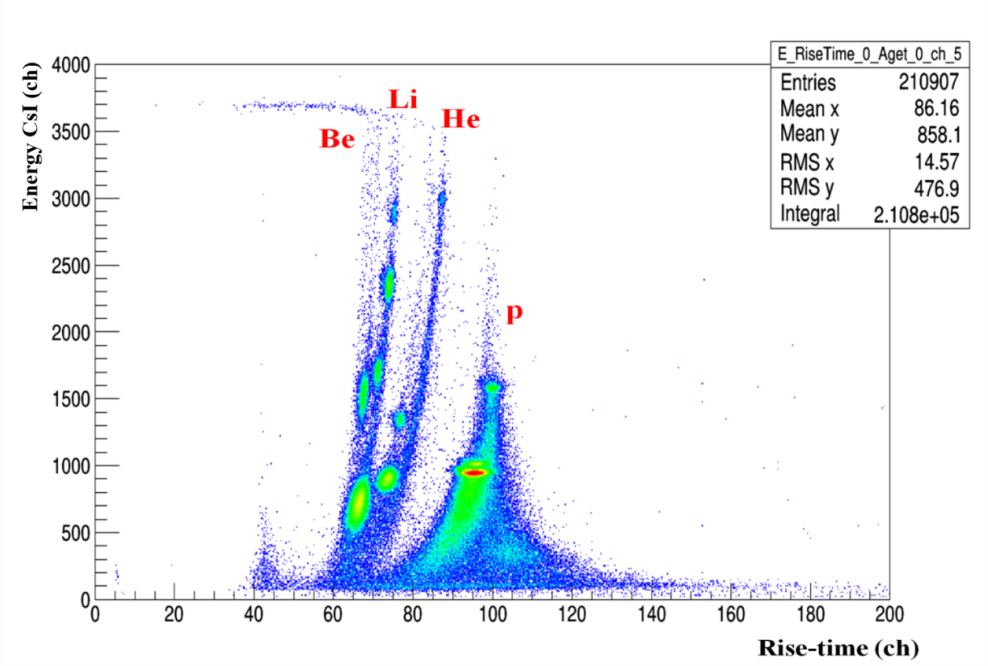

Figure 2.16: Example of Energy (Y) vs Rise-time (X) bidimensional histogram obtained with fragmentantion beam on CH_2 at 62 MeV. In this case, GET electronics was used at 50 MHz of sampling frequency.

To better understand the possibility of this identification method one can plot signals of different particles detected with equal energy. A selection of such signals is plotted in Figure 2.17:

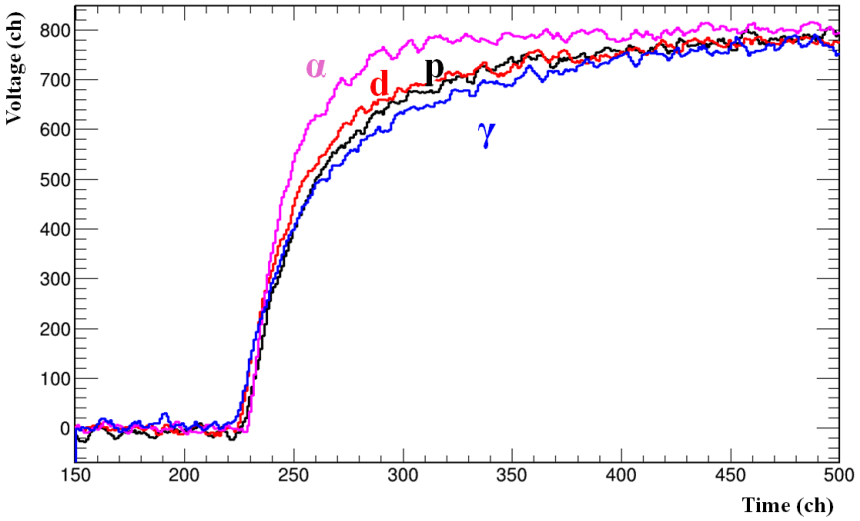

Figure 2.17: Collection of traces for different particles releasing the same light on CsI(Tl). The much faster light collection with α particles respect to deuterons, protons and γ-rays (or light elementary particles such as μ and π) can be well seen.

2.6.3 E-RiseTime for Silicon detectors

In Chimera we use the analog PSD with the method of two discriminators to measure the rise-time of particles stopped in Silicon detector and from this extract the particle charge (see paragraph 2.2.1). During the test performed with GET electronics it was not possible to have experiments with many particles stopped in Silicon detectors in order to check the feasibility of a similar method. However we performed a test, using a not depleted Silicon detector. In this way the electric field inside the detector is very low determined only by the junction, and the charge collection time is therefore very slow. The particle identification capability became very good, even if energy resolution is lost. In Figure 2.18 we show the result of this test.

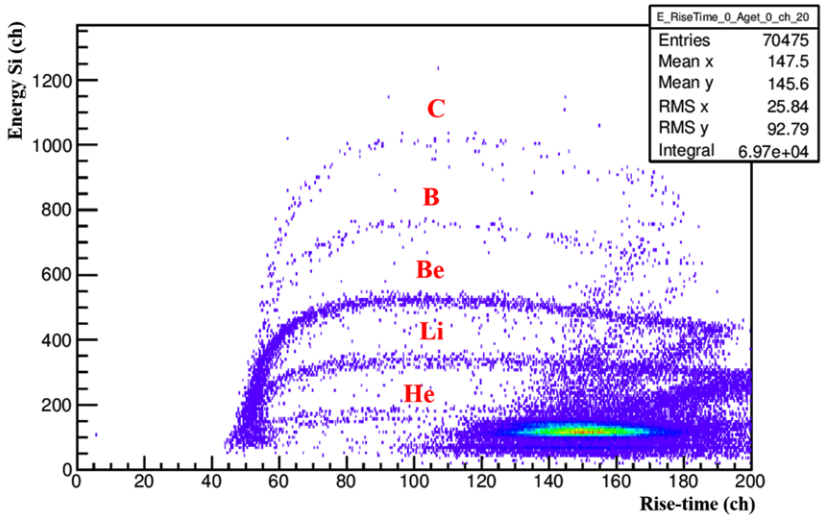

Figure 2.18: Example of Energy in Silicon detector (Y) vs Rise-time (X) bidimensional histogram obtained with fragmentantion beam on CH_2 at 62 MeV.

We note the beautiful charge identification obtained. We therefore conclude that GET electronics will be very good also for the measurement of charge of particles stopped in Silicon detectors via the method of pulse shape analysis of Silicon signal.

2.6.4 Fast-slow technique

The Pulse Shape Discrimination (PSD) technique is used in CHIMERA in order to identify particles stopped in the scintillator[1]; for high energy light particle, according to equation 2.1, ΔE signal becomes negligible thus it is not possible to use ΔE-E method. These particle are identified by means of the light signals collected by the photodiodes and sent into the relative electronic chain. In fact, the CsI(Tl) crystal, when excited by an incident particle, produces light mainly in two different types of physical processes,

[1]From 2008 the pulse shape technique was implemented also for the Silicon detectors, allowing the charge identification of less energetic particles that stop inside the first detection stage. Since the early 60s, it is well known that signal produce by ionizing particles detected in Silicon depends on both atomic mass A and atomic number Z of the particles [36, 37]

resulting in two distinct light output components, commonly named *fast* and *slow*, reflecting energy deposited by the particle in the crystal, and also the particle species. Fast and slow components are characterized by two different decay constants, τ_f and τ_s respectively. Such constants govern the temporal evolution of emission process, so that the output signal from CsI(Tl) is described by the combination of the two exponential components in the following expression:

$$V(t) = V_1 e^{-\frac{t}{\tau_f}} + V_2 e^{-\frac{t}{\tau_s}} \tag{2.4}$$

where $V(t)$ is the the light pulse amplitude at time t, V_1 and V_2 are the light amplitudes for the fast and slow components at time $t = 0$. The amplitude V_1 increases with increasing of stopping power $\frac{dE}{dx}$ of incident particles, so depending on their energy, charge and mass, while V_2 the is less sensitive to the incident particle species. This property of the CsI(Tl) crystal is the base of the pulse shape analysis.

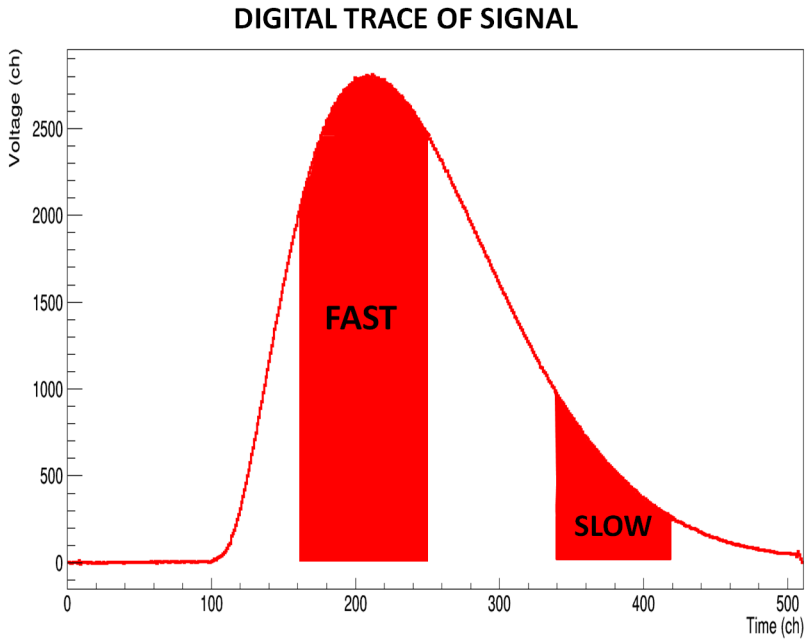

Figure 2.19: An example of integration of fast and slow components.

In Figure 2.19 we illustrate a case of fast and slow components of a signal. Knowing the combination of the two yields contained in the fast and slow

components it is possible to infer species and energy of the impinging particle. Another advantage of digital acquisition is the possibility of changing and/or move the gates of fast and slow components of signals to optimize the particle identifications.
However, the pulse shape analysis is not peculiar of CsI and Silicon detector but is quite a general technique and can be applied to other kind of detectors; we have also used this method during the Barriers experiment for the signals coming out from a Plastic scintillator.
The results will be shown in chapter 4.

Chapter 3

Tests with pulser and sources

3.1 New Data acquisition for FARCOS and CHIMERA

The data acquisition system (DAQ) for FARCOS takes into account the adoption of the GET project digital electronics described in the previous chapter. In addition, it allows for the coupling with the DAQ of CHIMERA 4π detector; beside it is thought to be flexible enough in order to be coupled with other possible existing DAQ system by assuming minor changes. Indeed, a part of CHIMERA itself (for CsI(Tl) detectors) will adopt the GET front-end electronics as main readout system. On the other hand the electronic and readout front-end (FEE) for Silicon (Si) detectors in CHIMERA (more recently upgraded for Si pulse-shape analysis [2, 38]) will stay bound to the current electronic chain that has, as final element, the analog codifiers (QDCs, Charge to Digital Converters and TDCs, Time to Digital Converter) housed in a VME bus. As a general rule, the data acquisition system for FARCOS allows for:

1. standalone readout for FARCOS detectors;
2. coupling the CHIMERA readout standard analogic (Silicon detectors) and digital acquisition (CsI(Tl) scintillators);
3. an easy coupling with others external devices (including CHIMERA).

This is done using a standardized frame buffer encapsulating the event data together with the basic information needed to merge the event data with

DAQ information coming from other devices (time-stamping and/or event numbering).The main task of data acquisition is to link the data flow coming from the front-end electronic (Readout) with the data Storage (see Figure 3.1).

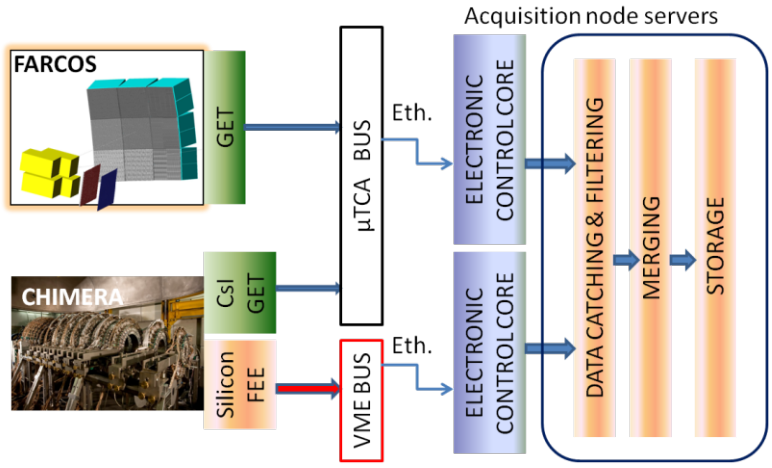

Figure 3.1: Schematic view of CHIMERA and FARCOS DAQ coupling. See text for details.

Intermediate tasks are data filtering, data analysis and on-line monitoring; these three last tasks are essential steps. They are crucial in particular for digital data acquisition where on-line pulse shape analysis (PSA) has to be applied to the digital samples in order to process the physical information from signals (energy, rise-time, time-of-flight, gated scintillators light components, etc). Final tasks are the merging of all the data belonging to the same event (event building) and data storing. Our choice in order to manage all these tasks is to use a hardware computing infrastructure (a farm of servers) where a distributed data acquisition framework NARVAL [39], developed at IPN Orsay, handles data flow and processes them among the different tasks described before. In this contest both the CHIMERA data readout and the GET one will be supervised and coordinated by the NARVAL system.
NARVAL is a modular, reconfigurable and distributed object oriented software for data acquisition, transport and filtering. It can coordinate different acquisitions as well handle the data flow through different acquisition tasks. The term "distributed" means that the tasks can run in one core of a specific

computer or in different computers of a computing farm using a CORBA equivalent inter-process communication.

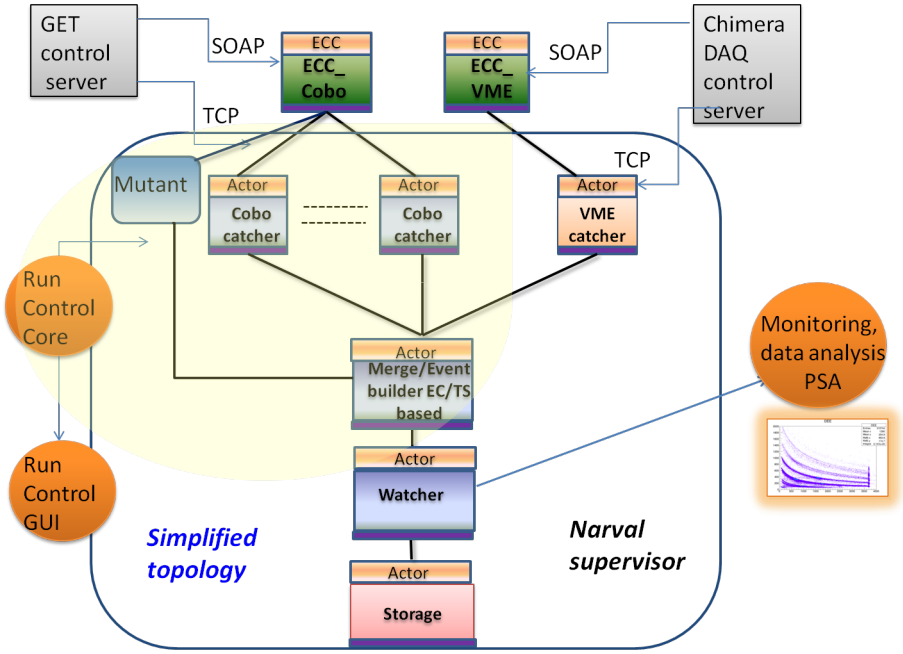

Figure 3.2: Simplified pictorial example of a NARVAL topology view for a setup with 2 CoBo(s) running with the GET Electronics and a VME data acquisition (CHIMERA). A topology is configured in NARVAL by defining a corresponding file in XML format.

The basic concept of NARVAL is the "actor". An actor handles buffered flow of data. It is an object class that can be interfaced with a specific code written in ADA95 or C^{++} producing a shared library. Figure 3.2 shows an example of a realistic topology when the coupling of GET and CHIMERA DAQ is envisaged. The Electronic Control Core (ECC) is the interface with the hardware for control and monitoring (for example in the initialization phase), communicating setup data and acquisition commands by means of Web services like the one defined by the SOAP protocol [40] using a client-server technology. For CHIMERA DAQ this new software component has of course to be implemented from scratch (CHIMERA SOAP Server) while it is already running for GET electronics. The actors called "catcher" collect the event data and distribute them for other tasks. The

intermediate actors ("watcher") send data to clients computers for example for PSA data analysis of the digitized sample or the spectra monitoring. The event builder ("merger") is an actor that collects data belonging to the same events on the basis of the time-stamp, the event number or both. The final task, in the example of Figure 3.1, is the data storage of the merged events. The Run Control Core (RCC) handles and coordinates all the common data acquisition activity and the status of the system. This is not part of the NARVAL software. In our tests with the GET electronics and NARVAL we have chosen to adapt to our needs the Run Control Core software developed at GANIL laboratory [41]. Together with the adoption of the NARVAL framework, this makes easier the planning of project for future common experiments with GANIL and other laboratories involving FARCOS and, in particular, it fulfils the main characteristic of FARCOS as a "highly transportable" detector array [6].

3.2 Set-up of GET electronics

As has often been said, GET is a fully digital electronics. This new device is able to manage thousands of electronic channels by remote control. As for any complex ACQ system, one must set many parameters to adapt the set-up to a particular experiment. In order to perform this task a program is available in the GET software package get-config-wizard.
In Figure 3.3 an example of use of this program is shown. In particular, we see some parameters needed to configure the CoBo modules. These parameters are applied to the all ASAD cards connected to the CoBo. For example, the "WritingClockFrequency", that can be set from $12\,,5\ MHz$ to $100\ MHz$, indicates the sampling frequency of the ASAD cards. For this reason we can use some CoBo for Silicon detectors (with $100\ MHz$ sampling frequency) and some CoBo (with $25-50\ MHz$ sampling frequency) for CsI(Tl) scintillators. Another important parameter is the "TriggerDelay". We set this parameter so that the start of the signals is from channel 100 on the x-axis. This is important because we use the first 100 channels for subtracting the pedestal to signals. When the "triggerMode" is "onMultlipicity" it means that we are triggering on the multiplicity of the events. Threshold is

settable with "multiplicityThreshold" parameter. To change the time period in which two or more events detected in different channels can be considered simultaneously we have to set the "moltWindowSize". This parameter sets the width (number of samples) of the multiplicity window (in units of 40 ns). For low multiplicity, for example if it is lower than 10, it can be ok to use a value of 1. Finally with "Generator" we active and set the internal pulser. With the ASAD[*] simultaneously all ASAD cards connected can be set, although, clearly, the setting of each ASAD can be changed individually, acting on ASAD[0] or ASAD[1] and so on. The same considerations are applicable at Aget and channel levels, as shown in Figure 3.4.

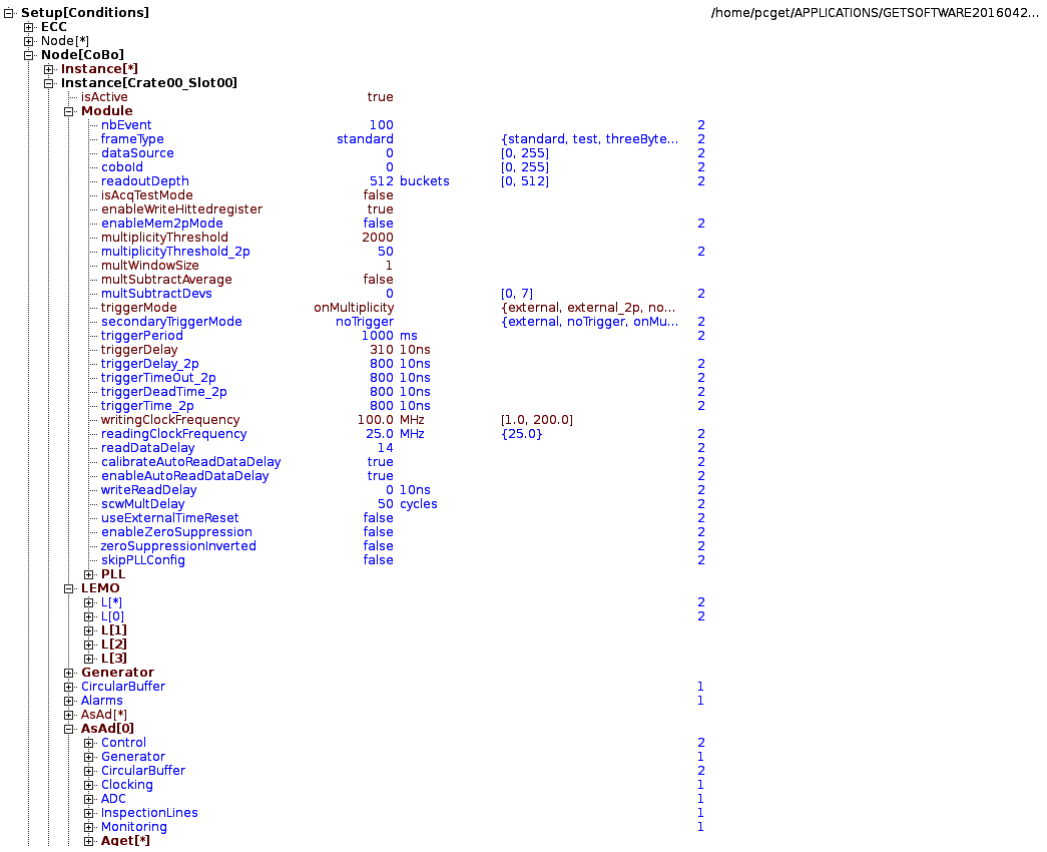

Figure 3.3: Screen of some parameters of a CoBo, settable by remote control.

Figure 3.4 shows parameters at Aget and channel levels. At the Aget level, when the "TestModeSellection" parameter is on "nothing", the input

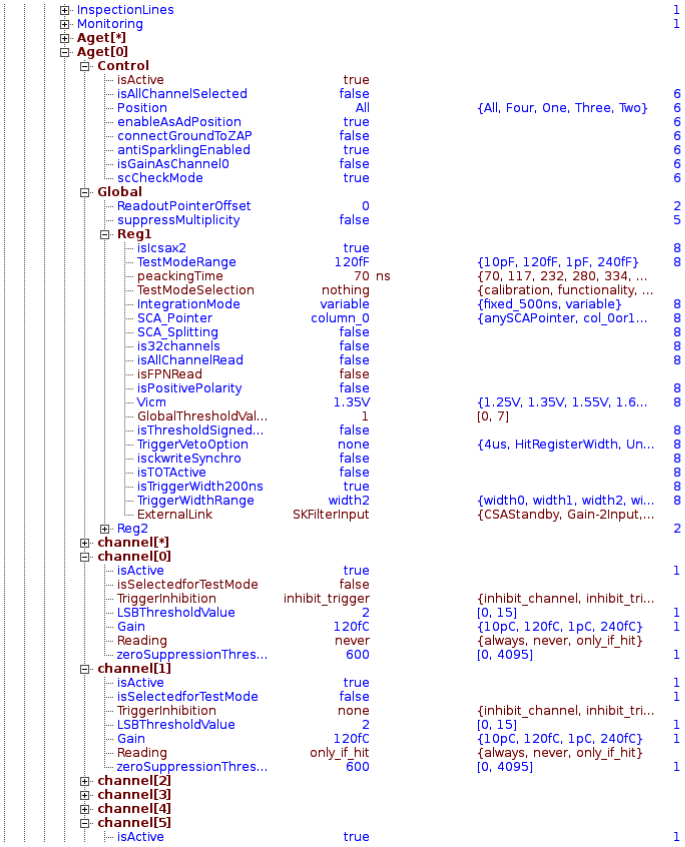

Figure 3.4: Screen of some parameters at Aget and channel levels, settable by remote control.

signal (in this case for the Aget[0]) is sent to:

1. CSA input if “ExternalLink” is on “none”;
2. SKfilter input if “ExternalLink” is on “SKfilterinput”;
3. ADC if “ExternalLink” is on “Gain-2 input”.

For tests with internal pulser “TestModeSellection” parameter must be on “functionality” and “ExternalLink” must be on “none”. The “peackingTime” parameter sets the characteristic of the internal pulser and the shaping time of SKfilter stage. It is, as just seen, settable with 16 values from 70 ns to 1014 ns.

The noise threshold is a programmable threshold value (7-bit DAC + 1

polarity bit). This value is set by 2 internal programmable DACs. The 4 bits of the first one "GlobalThresholdValue", common to the 64 channels, define the 3 MSB (Most Significant Bits) of the threshold value and the polarity of the input signal. The second DAC is attached to the channel and defines the 4 LSB (Less Significant Bits) of the threshold value.
At the channel level we can see, in Figure 3.4, the "Triggerinhibition" parameter that can be on:

1. "inhibit_trigger" if we want exclude the channel by the trigger;
2. "inhibit_channel" if we want exclude the channel (it is important to note that for a more stable multiplicity trigger a relatively large number of channels should be enabled to trigger);
3. "none" if we want the channel on and that it takes part to the trigger.

The "Gain" and "zeroSuppressionThreshold" will be not used in our case. Another important parameter is "Reading". It allows us to read the channel "always", "never" and "only if it". In this last case the channel is active but it storage the digitalized signal only if the amplitude signal exceeds the noise threshold. This option is important to reduce the transferred data and dead time.

To optimize GET acquisition we worked mostly on these parameters. To increase the ratio signal/noise we often adopted the SKfilter input. In this input stage, we used a peacking time of $1014\,ns$ for very noisy signals and peacking time of $502\,ns$ and minor ones for less noisy signals. However in case we do not want to perturb too much the original rise-time of the signal, a small peaking time should be used.

3.3 Linearity of the system and noise

In order to check the linearity and measure the noise threshold, we first did some preliminary test with internal and external pulser. We performed these tests using one ASAD card read by a reduced CoBo (see Figure 3.5) (test device based on a ML507 evaluation board of virtex5 FPGA).

Figure 3.5: The test system with one ASAD card and the Reduced CoBo.

The linearity (see Figure 3.6) and noise were compared to similar measurements performed using a 12 bit oscilloscope LECROY. We used the "Gain2" input in the AGET chip so directly converting the preamplifier signal without any filtering.

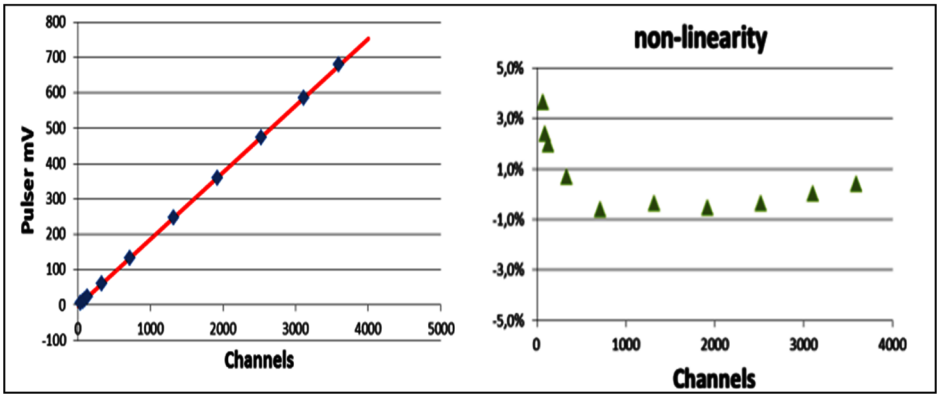

Figure 3.6: Linearity response of ASAD card.

The non-linearity measured is less than 1 % between 10 % and 90 % of the scale, being larger only at small values of the signals, where quantization errors probably influence such measurement. One has to note that the good linearity of the system allows us to calibrate the device with few points when we will transport the GET electronics in other laboratories. We

also compared the RMS noise, measured with the oscilloscope, with the standard deviation value of the peak measured with the GET electronics (see Figure 3.7). The behaviors observed are rather similar and compatible with calibration. We note that the higher noise measured for the largest value of the pulser amplitude seems more due to a saturation problem of the used set-up. Therefore, we have verified that the noise doesnt depend on the GET electronics.

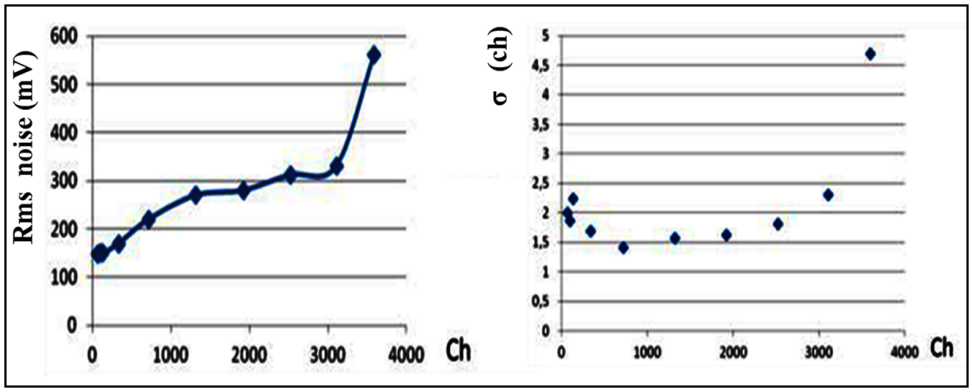

Figure 3.7: Noise measurements performed by oscilloscope (left panel) and Get electronics (right panel).

We performed other test, to verify thresholds behaviour, using both internal and external pulsers. The pulser signal, generated in the chip, is sent to the charge sensitive preamplifier (CSA) of the channel, then to the SKfilter, after to the memory based on a Switched Capacitor Array structure (SCA) and finally, if the signal is larger than the noise threshold, it is sent to ADC (one for each AGET).
We performed tests using 50 *MHz* sampling frequency on an AGET with only few activated input channels. We obtained a linear dependence between the discriminator threshold (in channels) and the pulse height necessary to trigger the system, as shown in Figure 3.8:

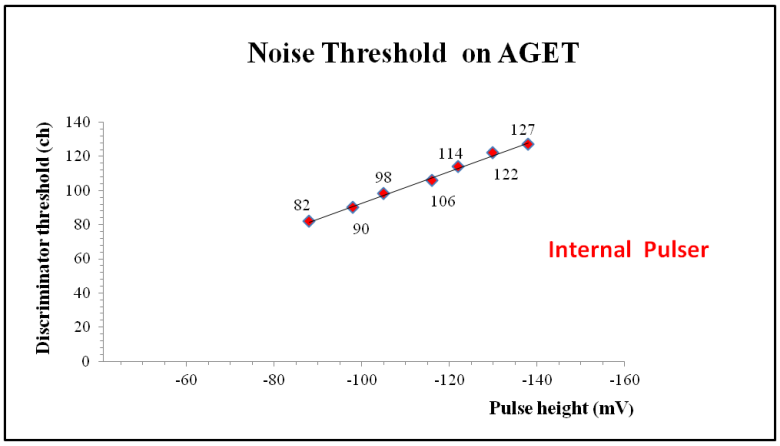

Figure 3.8: Noise threshold using internal pulser and reduced CoBo.

Afterwards, we tested the device with external signals. In this case, the "Gain2" input was used in the AGET chip so directly converting the signal without any filtering. The sampling frequency was again 50 MHz; also in this case, we activate only few channels of an AGET. However, in this case we had to add an offset $(+1.5\,V)$ to the signal; in fact skipping SCA a DC voltage level given by the internal preamplifiers fails and an external one is necessary for correct working of GET acquisition.
Also with external pulser we obtained a linear increasing trend for negative values of the voltage, as shown in Figure 3.9:

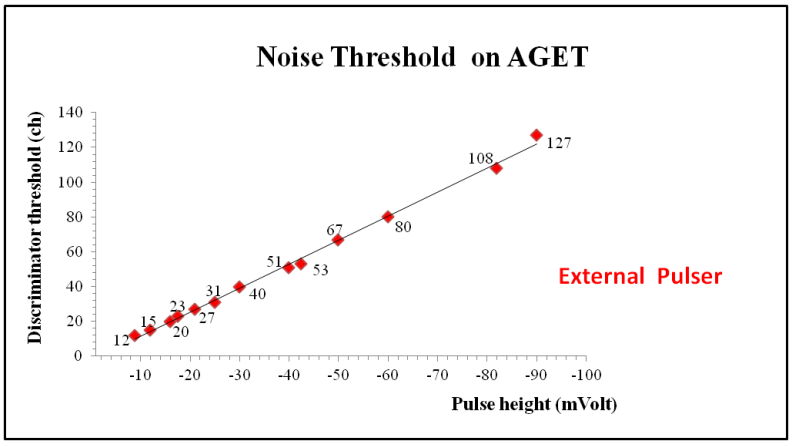

Figure 3.9: Noise threshold evaluated by using an external pulser and Reduced CoBo.

It is interesting to compare the discriminator threshold: the value of $-90\,mV$ for external pulser and the nominal $-140\,mV$ of internal pulser are cut by the same threshold of 127 units. This difference is due to the gain of the GET preamplifier (SCA) used with internal pulser, while in the case of the external pulser this stage (SCA) is skipped.

3.4 Multiplicity threshold

We have just seen how the noise threshold works. If the signal crosses the noise threshold, the discriminator output signal sets the hit channel register to an active level and forms, with the 63 others discriminator signals, a multiplicity signal (analogical sum). During the SCA writing phase, this signal is continuously digitized by the same external 12-bit ADC and analyzed on line to build a trigger signal. This multiplicity signal is an important feature for the AGET asic, since it informs that an event has been detected. The multiplicity trigger signal has also the property to be not a logical signal (two levels: "0" or "1") but an analog signal with amplitude proportional to the number of hit channels (64 possible values but this signal is summed at CoBo level for all ASAD cards and at the MUTANT level for all channels). To characterized the multiplicity threshold we conducted several tests using both the reduced CoBo with an ASAD card and internal pulser, and CoBo (see Figure 3.10) with 4 ASAD cards and external pulser. In both tests, we limited ourselves to investigate low values of multiplicity (from 1 to 10) because they are the ones for us physically important.

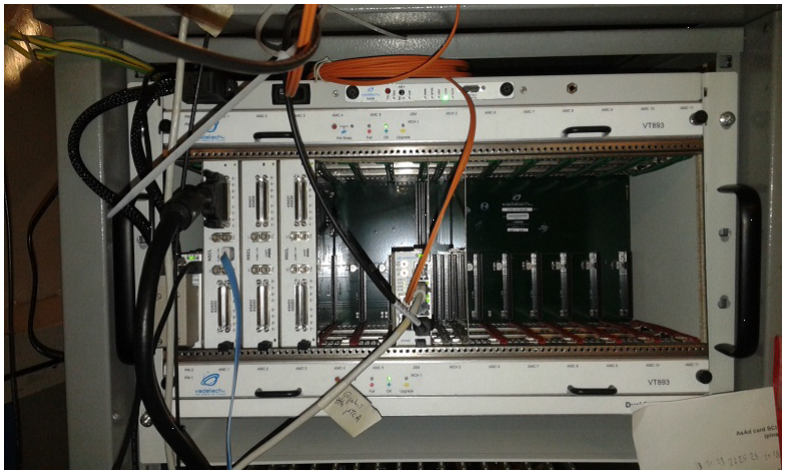

Figure 3.10: Photo of three CoBo board mounted in the microtca chassis.

By using the internal pulser set at 50 *MHz* sampling frequency, we obtained thresholds necessary to trigger the acquisition system with multiplicity rising from 1 to 10 channels on all AGETs with a linear trend and a step of 60 channels between two consecutive values of multiplicity as shown in Figure 3.11:

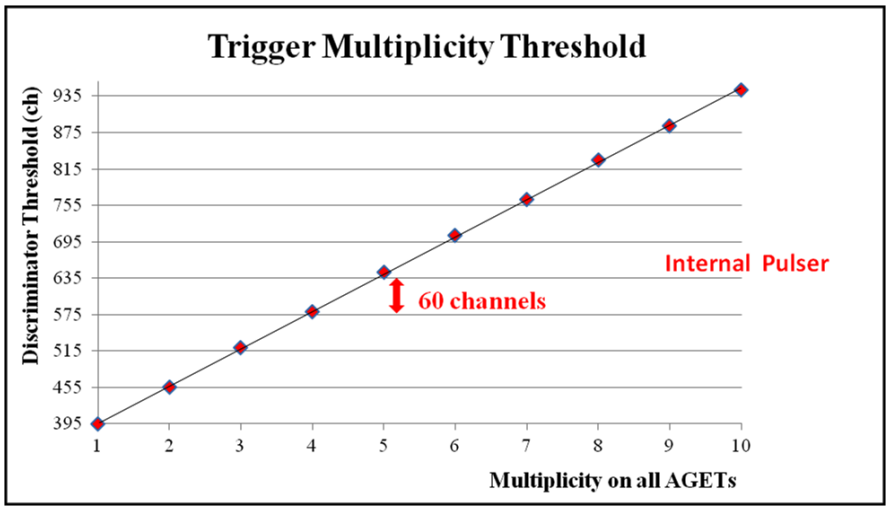

Figure 3.11: Multiplicity Threshold obtained with reduced CoBo and one ASAD card.

Using CoBo, we noted that the total multiplicity threshold depends not only by the ASAD card but also on the number of ASAD cards connected.

Moreover, in some cases, because of bad screening of some ASAD, it was very difficult to trigger with multiplicity 1. This problem is going to be solved with a new screen shown in Figure 3.12:

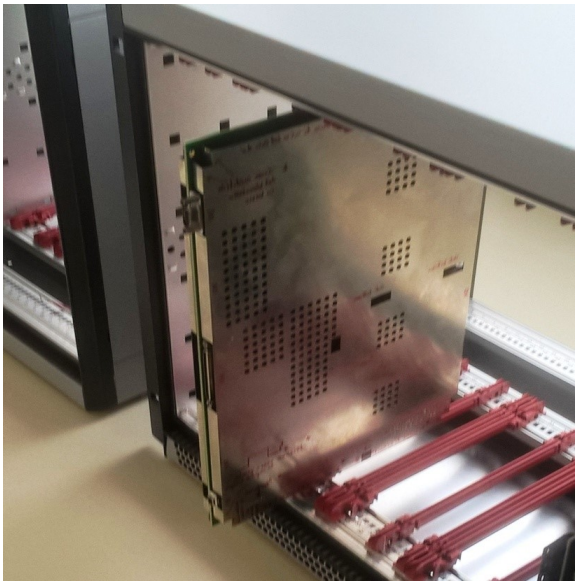

Figure 3.12: Photo of an ASAD card with a new screen for noise. The screen is made of ALPACCA, a copper-zinc-nickel alloys, having good mechanical characteristics and of corrosion resistance.

In Figure 3.13 it is shown an example obtained sending various copies of external pulsers to SKfilter input with 100 MHz sampling frequency.

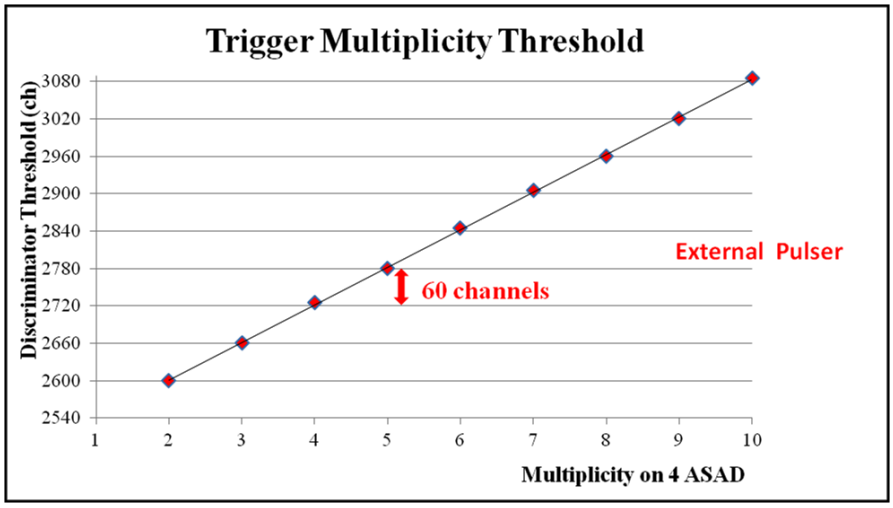

Figure 3.13: Multiplicity Threshold obtained with CoBo and four ASAD cards.

3.5 Tests with α-source and γ-rays on FARCOS and CHIMERA CsI scintillators

The alpha source tests were performed under vacuum using various CsI(Tl) FARCOS detectors (such tests were necessary to select the best crystals for the InKiIsSy measurement). After various attempts, we obtained the best results by improving the technique for data analysis. We chose a triangular filter software (see paragraph 1.4) 321 taps wide. Figure 3.14 shows the result of this procedure with a spectrum measured using a "mixed nuclides" (Pu, Am, Cu) α-source detected in one of the best performing CsI(Tl) FARCOS detector.

We note that the FWHM of each peak is of the order of $4-5$ channels corresponding to about $180\,keV$. We underline that the quantization error is already of the order of $50\,keV$. Therefore the result is rather good, for a CsI(Tl) detector, taking into account that the full dynamics is about 200 MeV alpha energy equivalent, very good for large part of the CHIMERA detectors.

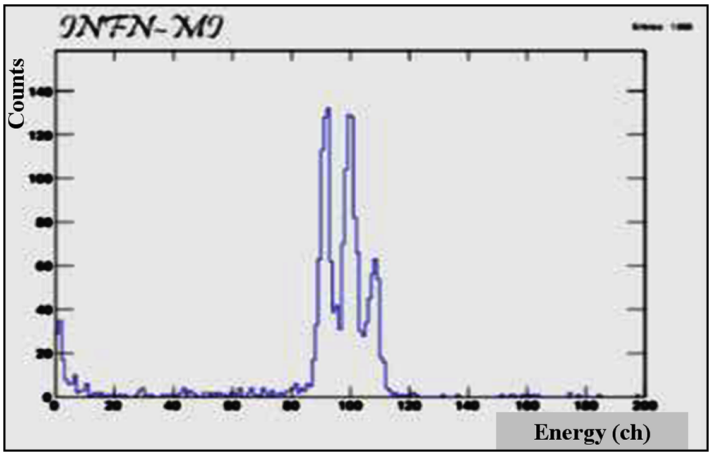

Figure 3.14: Calibration α-source as seen by using CsI(Tl) FARCOS detector with GET electronics.

We also performed tests using γ-ray sources in particular: a ^{60}Co source and an *Am-Be* source. We know that the ^{60}Co source emits two correlated γ-rays at 1.17 and 1.33 MeV. The left panel of Figure 3.15 shows that we are unable to discriminate the two γ-rays; this observation is consistent with a resolution not better than 10 % (that is more or less what we expect from a CsI(Tl) scintillator read by photodiode), but again at least 3 % is due to the quantization error.

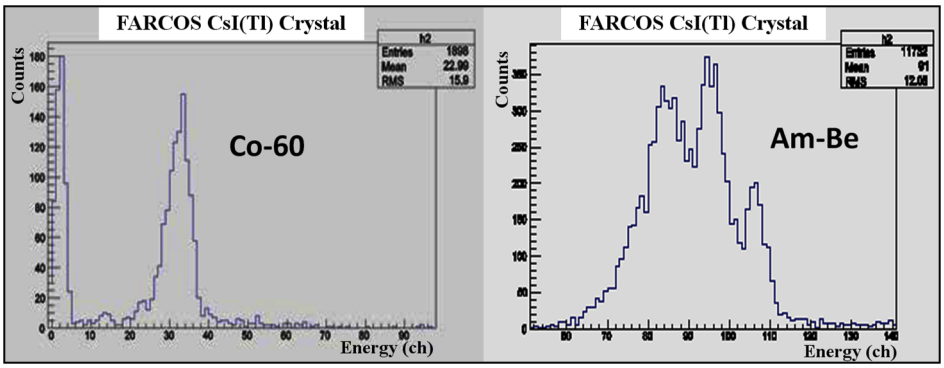

Figure 3.15: (Left panel) spectrum of a ^{60}Co γ-ray source as seen through a FARCOS CsI(Tl) crystal with GET electronics. (Right panel) the 4.44 MeV γ-ray from *Am-Be* source as seen through the same detector[1].

For the *Am-Be* source we should see the 4.44 MeV γ-ray due to the

de-excitation of the first excited state of ^{12}C. In effect, we see in Figure 3.15 (right panel) the full energy, first and second escape peaks[1].
We performed similar test also for some CHIMERA CsI(Tl) scintillators. First, the source was positioned behind the scintillator, at $5cm$ from photodiode. We used a Reduced Dual Gain module (for more details see chapter 2) with gain $8\times$. GET electronics were used with 25 MHz sampling frequency and SKfilter input with shaping time of $1\,\mu s$. 201 taps for software filter to determine the maximum of signals and 17 taps for the software filter to determine the rise-time were also used. As shown from the Figure 3.16 (left panel), thanks to the gain of Reduced Dual Gain module we are able to discriminate the *Am-Be* sources, but we do not distinguish the three peaks as obtained with FARCOS CsI(Tl). This worsening of the resolution is due to the much larger size of the CHIMERA crystal relatively to the readout photodiode (same size than the one used for FARCOS), and to the better quality of CsI(Tl) scintillators of FARCOS (perhaps also due to the age of the wrapping material).

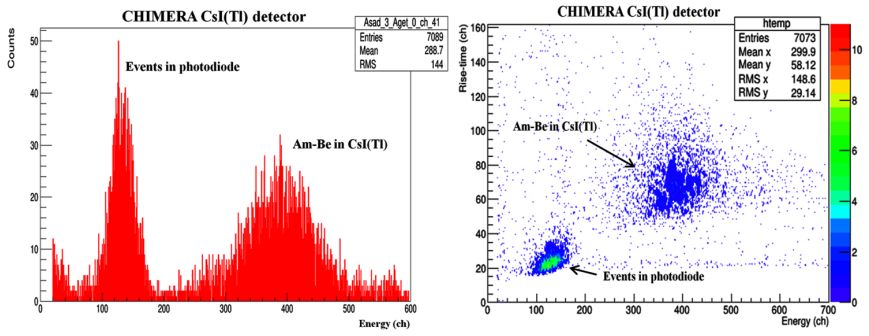

Figure 3.16: (Left panel) Spectrum with *Am-Be* source as seen in a CHIMERA CsI(Tl) crystal with GET electronics. (Right panel) Rise-Time vs Energy bidimensional histogram of the same detector. In this case, one channel is equal to $40\,ns$ for Rise-time axis.

Moreover, in the left panel we notice another peak at approximately

[1]We remember that, in the detection of a high energy γ-ray the dominant effect is couple creation. The β+ created in the event annihilate soon, emitting two γ-rays of $511\,keV$. These γ-rays can be detected both inside the scintillator, creating the full energy peak, or one or both can escape, producing the first and second escape peaks.

130 channels, due to events detected directly in the silicon photodiode. These signals are in fact faster than the ones coming from the CsI(Tl) therefore cannot be γ-rays as shown in the Rise-time vs Energy bidimensional histogramm (Figure 3.16 right panel). Another test has been conducted in the same conditions of the previous one except for the source and sampling frequency of GET, in fact we used a ^{60}Co source and GET with 50 MHz sampling frequency, in order to test electronics in these conditions.

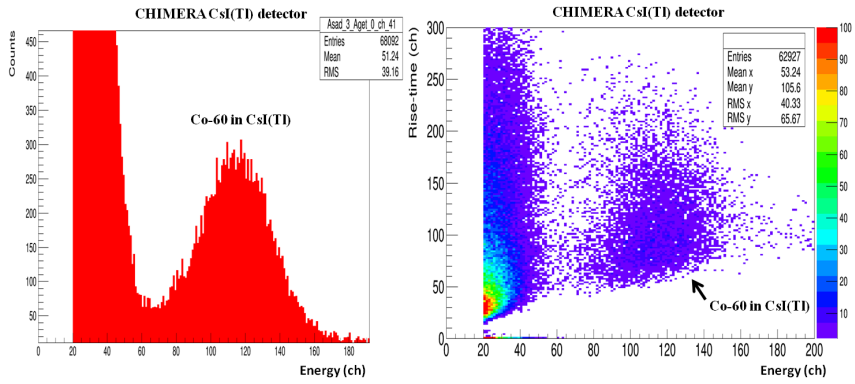

Figure 3.17: (Left panel) Spectrum with ^{60}Co source as seen through a CHIMERA CsI(Tl) crystal with GET electronics. Source 5 cm to back of scintillator. (Right panel) Rise-time vs Energy bidimensional histogram of the same detector. In this case, one channel is equal to 20 ns for Rise-time axis.

As shown in Figure 3.17 (left panel) thanks to Reduced Dual Gain we are able to discriminate the ^{60}Co in CHIMERA CsI(Tl), but the resolution of scintillator doesnt allows to distinguish the two peaks, at 1173.2 keV and 1332.5 keV, of ^{60}Co source. The right panel shows that the peak at about 120 channels in the left panel are ^{60}Co. However in this case the range of rise-time of ^{60}Co γ-rays is more large (from 50 to 180 channels) that the previous case. This behavior is due to the difficulty of triggering at low energy, close to the noise threshold.

3.6 Tests with α-source on strip detectors

We performed also tests on FARCOS DSSD detectors under vacuum conditions with a mixed nuclide alpha source. We used, for this test, 32 channel preamplifiers with pseudo-differential output realized by INFN-MI. This enable us to use twisted pairs flat cables for the data transmission. A differential receiver was used at the end of the cable to feed the signal in the ASAD card. The Gain2 input and external trigger were used for GET electronics.
Using 321 taps for triangular filter to determine maximum of signals we get the best results. In Figure 3.18 the energy spectrum obtained is shown. Due to the preamplifier gain (10 mV/MeV) the dynamic range is about 100 MeV. The measured resolution is about $60 keV$ with $3-4$ channels of FHWM on average in the different peaks.

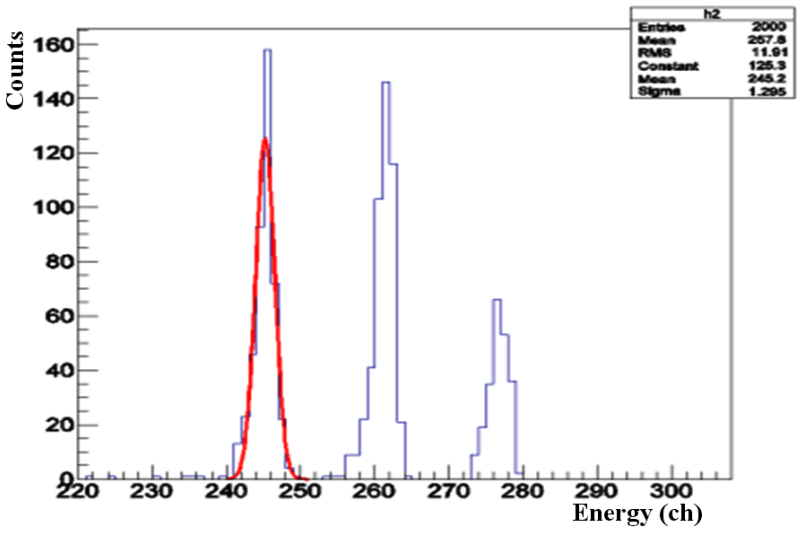

Figure 3.18: Calibration α-source as seen through FARCOS DSSD detector and GET electronics.

3.7 Tests with high-purity Germanium (HPGe) detector

In the previous paragraphs we have described many tests performed with silicon and CsI(Tl) detectors used for FARCOS and/or CHIMERA. The intrinsic energy resolution of such detectors, with the used preamplifier gain, is not good enough to evidence the limits of the electronics. Therefore, we performed some test with a very performing detector, a high-purity Germanium (HPGe), available in Messina. In this way, we also checked the simple transportability of GET electronics.

Because of small bandgap ($0.7\,eV$), room-temperature operation of Germanium detectors of any type is impossible because of the large thermally induced leakage current that would result. Instead, Germanium detectors must be cooled to reduce the leakage current to the point that associated noise does not spoil their excellent energy resolution. In our tests, the temperature was reduced to $77K$ through the use of an insulated dewar in which a reservoir of liquid nitrogen was kept in thermal contact with the HPGe detector.

The dominant characteristic of germanium detectors is their excellent energy resolution when applied to γ-ray spectroscopy. The great superiority of the Germanium system in energy resolution allows the separation of many closely spaced γ-ray energies, which remain unresolved in the CsI(Tl) spectrum. We took advantage of HPGe detector quality to investigate GET electronics resolution, and, at the same time, to perform a better analysis of the used software filters.

To have a reference for the evaluation of GET electronics, we acquired the γ-rays emitted from ^{60}Co and ^{88}Y sources using both MAESTRO (digital acquisition with 14 bits of resolution), and GET Electronics (12 bits of resolution but with full pulse shape digitization). The signals, coming out from germanium preamplifier, were digitized with GET at a frequency of 50 *MHz*. We used a $502\,ns$ shaping time in the SKfilter stage of AGET chips; while in MAESTRO digital acquisition, also an amplifier (ORTEC 572 with shaping time of $2\,\mu s$) was used. In the Figure 3.19, Figure 3.20, Figure 3.21 we compare the energy of two peaks of ^{60}Co and ^{88}Y obtained with

both GET and MAESTRO acquisitions. In this figure, we show the result obtained using 251 taps for the GET software filter.

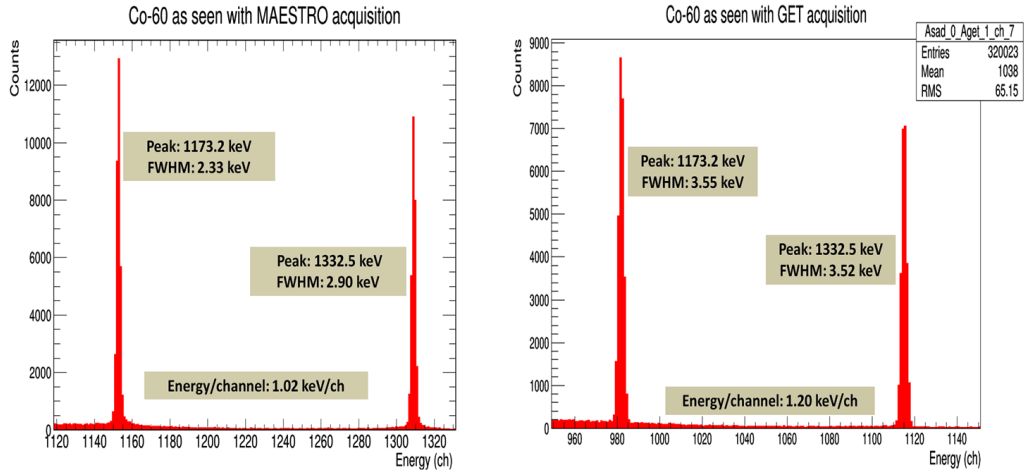

Figure 3.19: Peaks of ^{60}Co at 1173.2 keV and 1332.5 keV obtained with both MAESTRO acquisition (left panel) and GET acquisition (right panel).

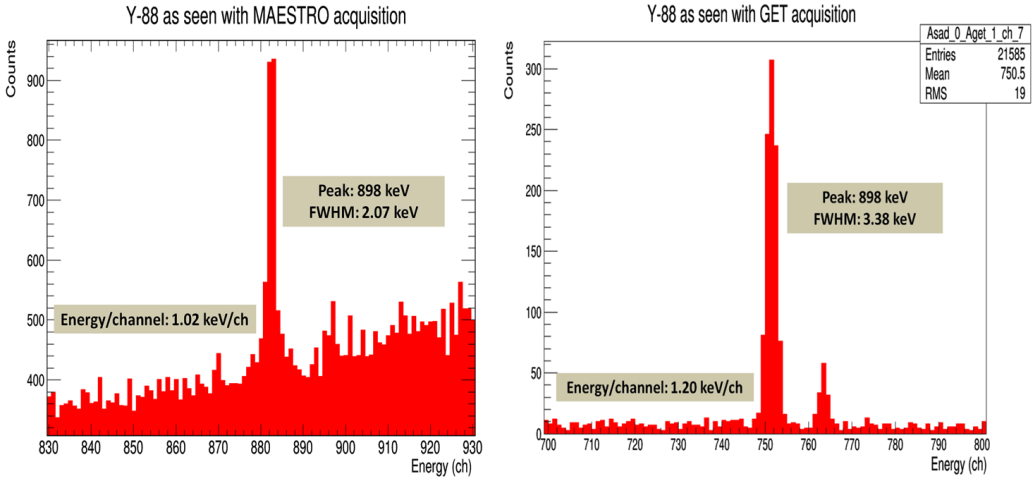

Figure 3.20: Peak of ^{88}Y at 898 keV obtained with both MAESTRO acquisition (left panel) and GET acquisition (right panel). In this case with MAESTRO we have more background due to Compton effect of the ^{60}Co peaks. In fact, with MAESTRO, we acquired at same time both ^{60}Co and ^{88}Y. With GET, instead, a source at a time was acquired.

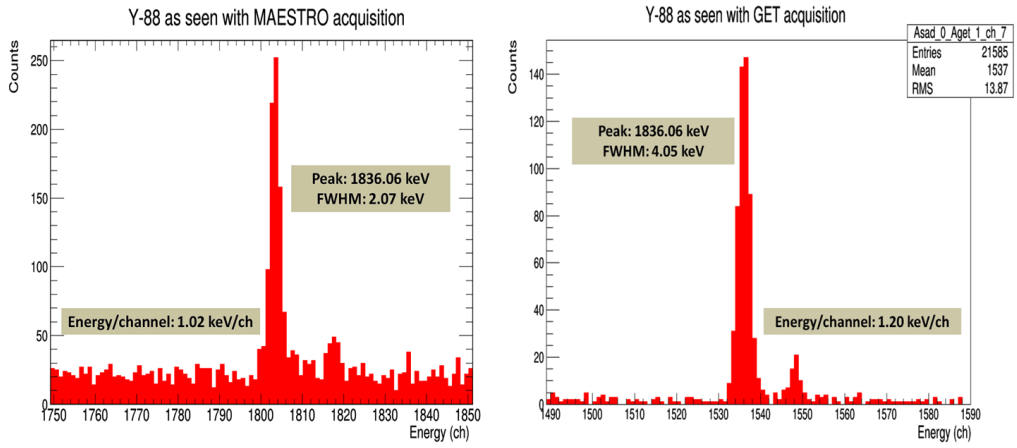

Figure 3.21: Peak of ^{88}Y at 1836.06 keV obtained with both MAESTRO acquisition (left panel) and GET acquisition (right panel).

As shown in the figures above, the resolution of GET is comparable to that of MAESTRO. This is a very beautiful result showing the intrinsic quality of GET electronics, notwithstanding the smaller number of bit available, thanks to the digitalization of the signal and the software filters that can be applied, we get a worsening in the resolution smaller than 1 keV. The smaller bit number is in fact somewhat compensated by the full digitization of the signal producing a larger effective amount of bit.
Moreover, as shown in Figure 3.22 the linear energy calibration passes exactly through zero point (see equation of the fit) as it should be since we subtract, event by event, the pedestal.

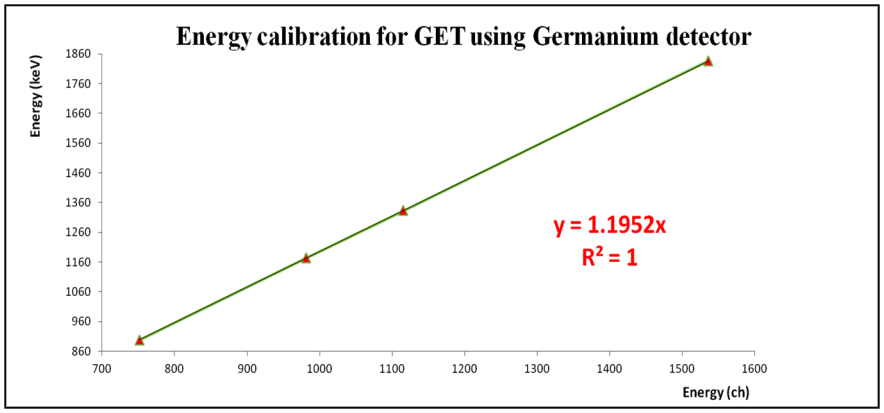

Figure 3.22: Energy calibration of GET electronics using the two peaks of ^{60}Co (1173.2 keV and 1332.5 keV) and the two peaks of ^{88}Y (898.04 keV and 1836.06 keV).

3.8 Characterization of software filters developed to determine the signal amplitude

In order to characterize the behavior of the software filter developed in order to determine the signal amplitudes, varying the number of taps, we conducted several analysis offline on acquired data. In previous paragraphs, we presented only the best-chosen results. In this paragraph, we want to better analyze the filter effect showing the dependence of the obtained results from the adopted filter. First, we show some analysis of data taken during CLIR experiment, (see next chapter).

One has to take in mind that when resolution is too low the filter software cannot improve too much the results. For instance, we analyzed data of Fragmentation Beam at $\sim 50\,AMeV$ on CH_2 target. In this experiment, we used GET electronics (a CoBo and two Asad cards) and, for these data, a frequency sampling of 25 MHz with a SKfilter input (1 μs of shaping time) for a CHIMERA telescope (Ring2 telescope N°18-E). As shown in Figure 3.23, increasing the number of taps (from 211 to 401) the peak position relative to the protons detected in CsI(Tl) decreases. The reason of this behavior will be clearer later in this paragraph. The observed FWHM of the peak (Full Width at Half Maximum $\sim 2,355\,\sigma$) depends slightly from the

used taps number. We note a first minimum at 271 taps, and a second one around 351, but they are inside the error bars. In this case, the kinematical spread of the peak and the relatively poor resolution of the CsI(Tl) does not allow us to appreciate a large effect of the number of software filter taps on resolution.

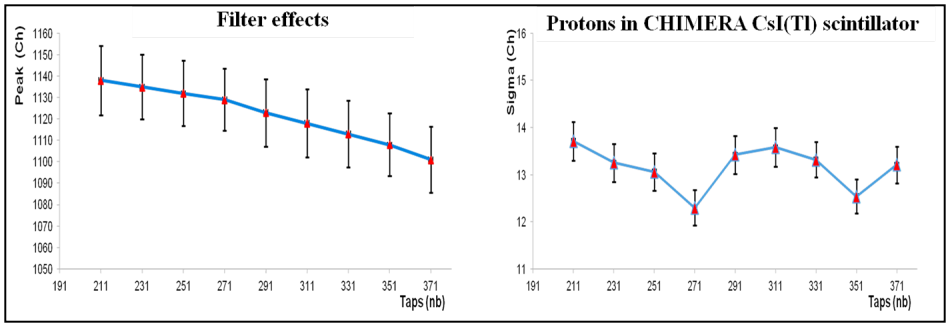

Figure 3.23: Trend of the peaks (left panel) of the proton signals in CsI(Tl) scintillator and of sigma (right panel) with increasing the number of points (from 211 to 371 taps) of the software filter used to determine the signal amplitude of detected particles.

We also considered the relative resolution, in particular the resolution normalized to the peak value as shown in Figure 3.24. How can we see, relative resolution has the same trend of sigma and does not vary significantly because the peak position dependence from the taps number is relatively narrow (the peak decrease of about 40 channels with the increasing of the number of taps as shown in left panel of Figure 3.23). The first minimum is smaller than the second one however error bars are too large to get a conclusion.

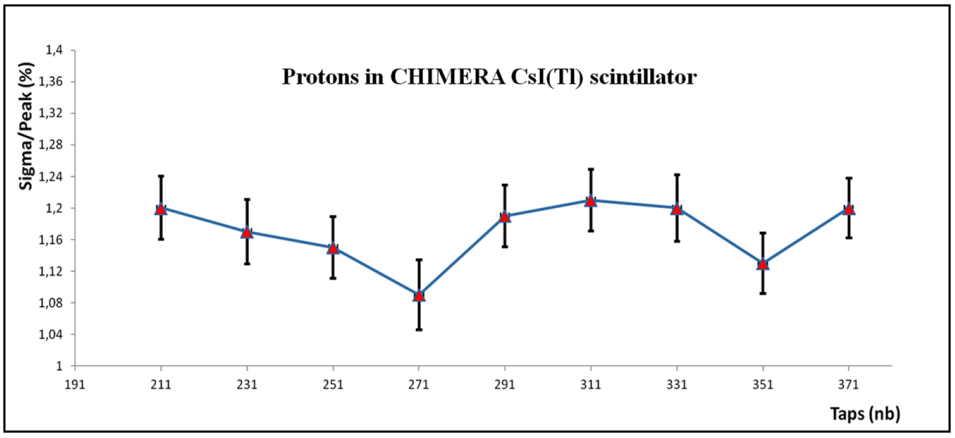

Figure 3.24: Trend of the resolution (normalized to the peak value) as a function of taps number in CsI(Tl) case.

After, we analyzed the data of a Silicon detector, less noisy than a CsI(Tl) and so with a better resolution. We analyzed offline the data of SIKO experiment. In particular, we analyzed data of ^{16}O at 160 MeV on ^{12}C target collected at 4.1°. In this experiment we used GET electronics (a CoBo and four Asad cards) and, for these data, a sampling frequency of 50 MHz with a SKfilter input (1 μs of shaping time). Even if the Silicon resolution is better than the one of CsI(Tl), however in this case the kinematical spread produce again a large peak.
The Figure 3.25 shows again that, also in this case, increasing the number of taps the peak position decreases. FWHM (Full Width at Half Maximum $\sim 2,35\,\sigma$) seems to decrease more than in previous case, however the error bar are still large and does not allow a definite conclusion. Again it is important to check the relative resolution therefore we show in Figure 3.26 the FWHM normalized to the peak position.

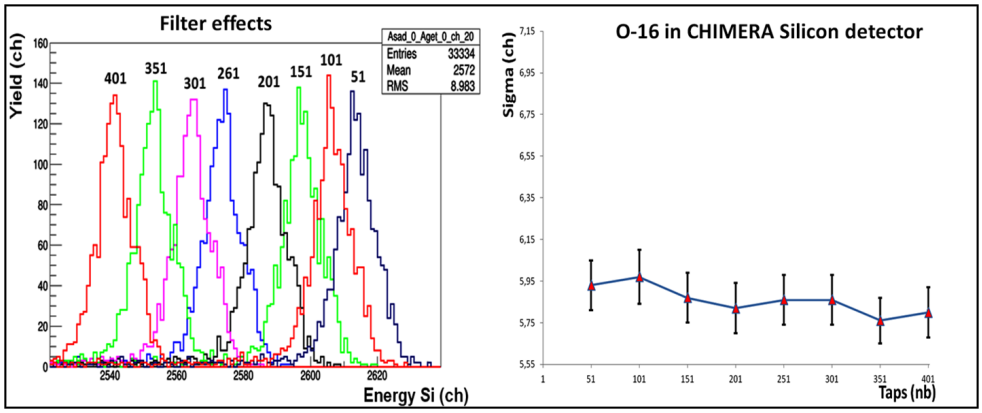

Figure 3.25: Trend of the peaks (left panel) of the elastic scattering of ^{16}O signals detected at 4.1° in Silicon detector and of sigma (right panel) with increasing the number of points (from 51 to 401 taps) of the software filter used to determine the signal amplitude of detected particles.

In this case like in the CsI(Tl) one, some fluctuations are enhanced but again the error bars does not allow definite conclusions.

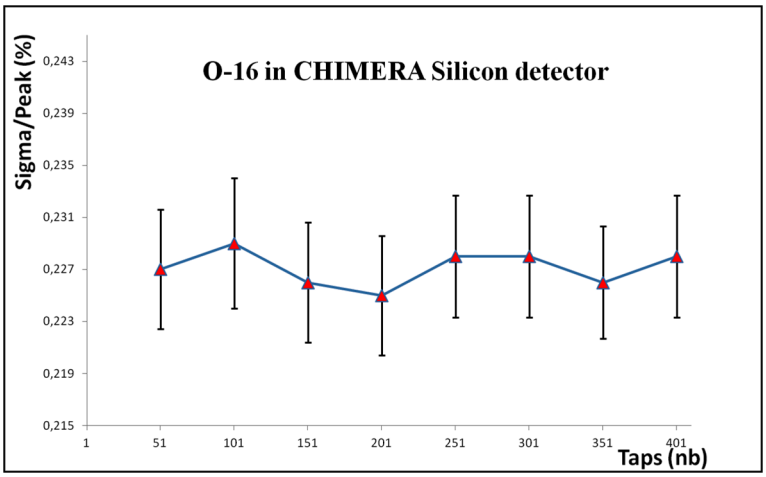

Figure 3.26: Trend of the resolution normalized to the peak value for the signals of the elastic scattering of ^{16}O signals detected at 4.1° in Silicon stage.

Finally, we worked (experiment that we have just described) on data of ^{60}Co and ^{88}Y γ-rays obtained with GET electronics (reduced CoBo and one ASAD card) using a Germanium detector. The Figure 3.27 shows the results

obtained.

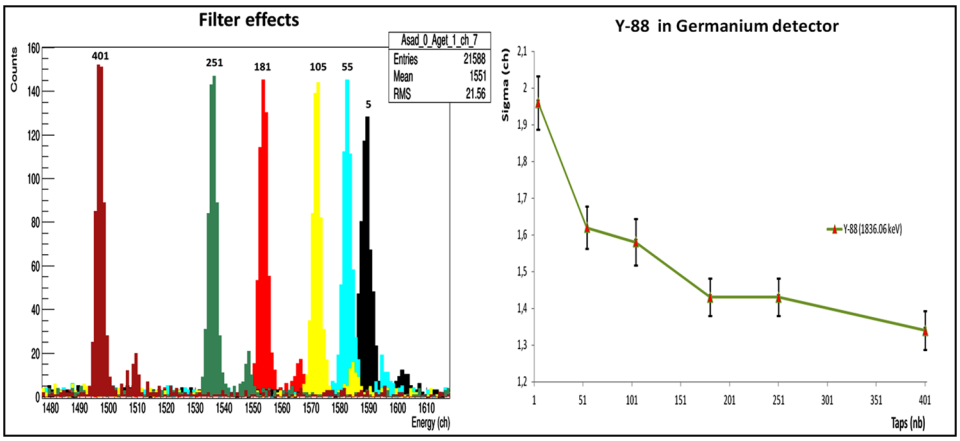

Figure 3.27: Trend of the peaks (left panel) of the ^{88}Y ($1836.06\,keV$) signals in Germanium detector and of sigma (right panel) with increasing the number of points (from 5 to 401 taps) of the software filter used to determine the signal amplitude of detected particles.

Again we note that increasing the taps used for the software filter the extracted maximum of the signal decrease. In this case, because of the good energy resolution, we are also able to extract a good peak value using a very small 5 taps filter. We note that increasing the numbers of taps the resolution of the peaks improves but the gain is not very large over 100 taps. This is confirmed by the analysis of the relative resolution (see Figure 3.28) that with a smaller error bar than in previous analysis shows that it is not really necessary to increase very much the number of used taps in the filter to get a reasonable result. In effect increasing the number of taps increases the CPU time needed to perform the calculations. It is therefore important to reduce as much as possible this number to speed up data analysis.

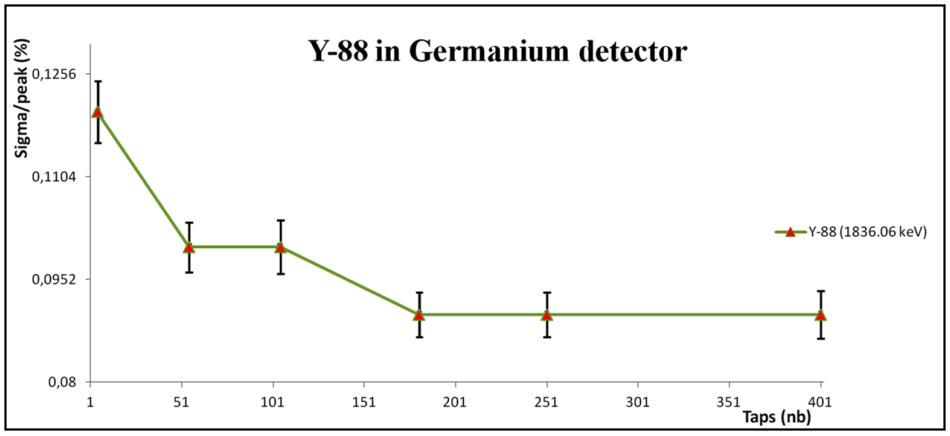

Figure 3.28: Trend of the resolution normalized to the peak value in Germanium case.

In conclusion, taking into account the previous results, we will use filters to determine signal amplitude with not more than 250 taps. This is also important in order to do not reduce the effective dynamics of the system as it happens due to the shift to smaller value of the maximum of the peak. One can better understand the filter effect looking to the plots in Figure 3.29 where the digitized signal is shown together with the filtered one. As shown in the Figure 3.29 with just a few taps (5) the filtered curve adapts perfectly to the signal but in this case, we have (as already seen) a worse resolution because the filter is not able to completely cut the high frequency noise of the signal. In the case of more taps (i.e. $151 - 251$), the noise is filtered and the signal is reasonably well reproduced. However, putting too many taps (i.e. 351) the filtered curve completely miss the maximum of fast signals.

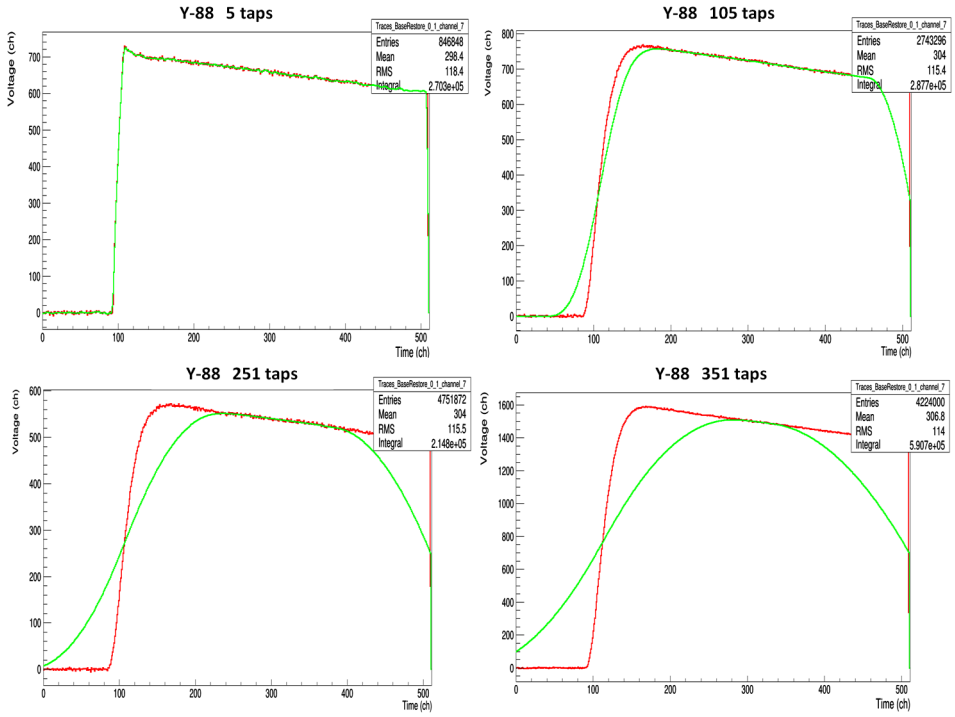

Figure 3.29: Illustration of ^{88}Y signals (red lines) and software filterered ones (green lines), used to determine the maximum of signals, obtained increasing the numbers of taps.

While as shown in the Figure 3.30 for slow signal, like gamma ray detected in CsI(Tl), we can see how with a software filter of 105 taps, we are able to well extract the maximum, at around 400 channel (time).

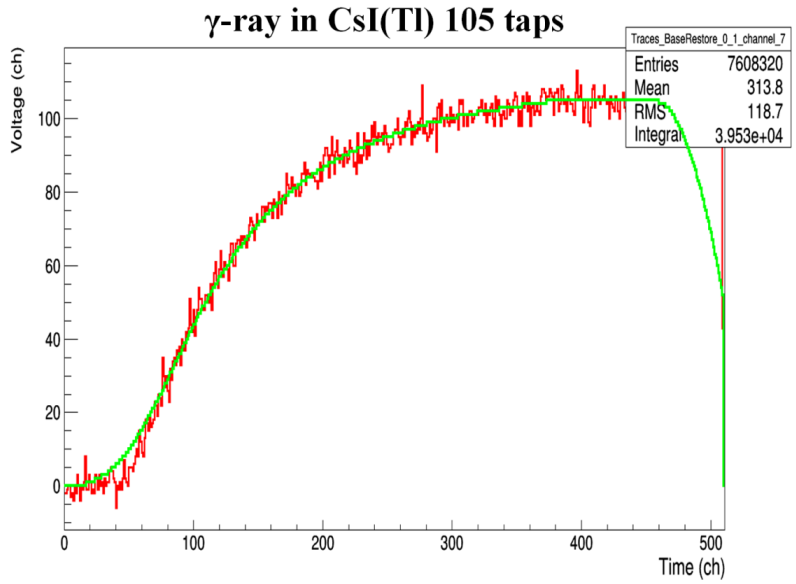

Figure 3.30: Illustration of γ-ray signal (red lines) in CsI(Tl) and software filtered one with 105 taps (green lines), used to determine the signal amplitude.

Taking into account these considerations we will use software filters to determine the maximum of signals with about $100-200$ taps; though, thanks to the storage, we can change offline the numbers of taps, in order to have the best configuration for the experiment data.
Clearly, as shown in Figure 3.31, not all the detected signals are good signals, due to many reasons, such as detector malfunction or pile-up. For these signals, the filter analysis produces incoherent results, missing the maximum; but, looking to other variables, like rise-time or time-zero, we can investigate on these data and reject them.

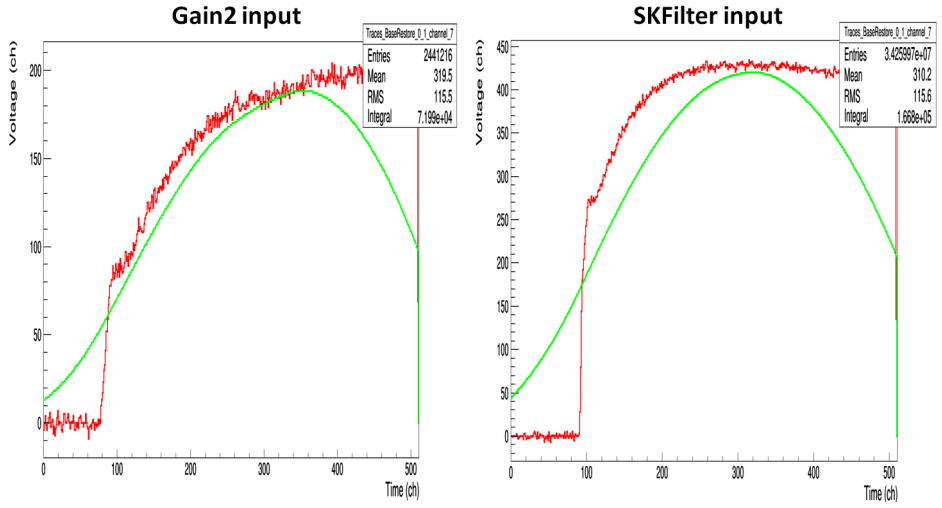

Figure 3.31: Example of signals in Gain2 input and in the SKfilter stage. In these cases the signals (red lines) are not good and also filtered ones (green lines) do not fit well to the signals.

3.9 Tests on time resolution

In order to check the time resolution of GET electronics we conducted some tests using NIM signals. We used various sampling frequency and SKfilter input with $70 - 140\,ns$ in order to well detect the beginning of the signal. We have measured the difference in the arrival time of the signal between different channels. More in detail we have measured this time difference between channels belonging to the same AGET, to the same ASAD, and to different ASAD cards read by the same or by a different CoBo.

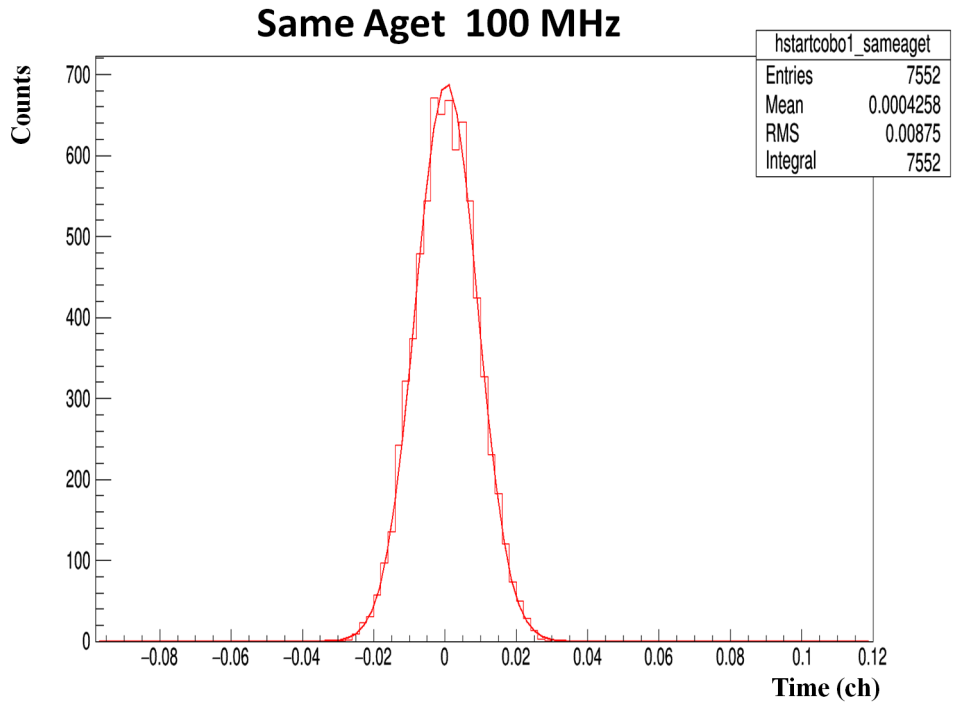

Figure 3.32: Time difference of two copies of a NIM signal detected in the same AGET. For x-axis 0.01 channel = 100 ps.

Figure 3.32 shows the best result obtained in the case of signals belonging to the same AGET at 100 MHz and with 70 ns SKfilter peaking time. In this case, we obtained a time resolution (sigma) of 90 ps. A little bit worse resolution is obtained in the case of 50 MHz, 140 ps. A little degradation of the resolution is also obtained measuring the coincidence time between channels belonging to different AGET. A bad result is obtained when the coincidence time is measured between channels belonging to ASAD cards read by different CoBo (see Figure 3.33).

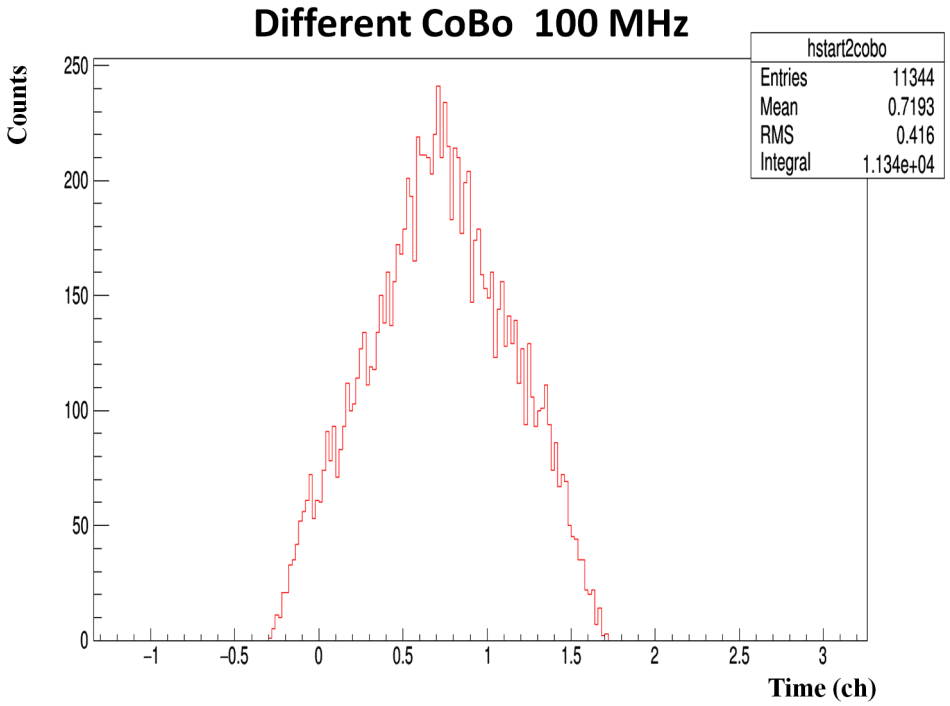

Figure 3.33: Time difference of two copies of a NIM signal detected in two different ASAD cards read by different CoBo. For x-axis 1 channel = 10 ns.

The distribution is no more Gaussian but more triangular and FWHM is of the order of the step of digitization of the signal, 10 ns at 100 *MHz*, 20 ns at 50 *MHz*. The very good result in the time resolution that can be measured at 100 and even at 50 *MHz* allow the use of GET electronics for timing measurements, as for the acquisition of the tagging system of fragmentation beams. This result was expected and is similar to what observed with other digital ACQ systems [42].
The bad result obtained in the case of channels belonging to different CoBo, means that an improvement of the synchronization between the different CoBo cards must be performed. While waiting for solution with improvement of the firmware, a simple solution can be given using one reference signals sent to one of the channels of each CoBo used.

3.10 Dead time measurements

Another important parameter of any ACQ system is the dead time. We have just seen in chapter 2 how GET electronics is constituted. For each channel the waveform of 512 consecutive samples (each one stored in a 32 bit word length) is collected from ADCs (whatever is the sampling frequency, from 1 to 100 *MHz*) and constitutes the final sampled signal. The readout of ADC outputs is performed by the CoBo module firmware that can receive inputs from a maximum of 4 ASAD cards corresponding to 68 (64 electronic channels + 4 FPN)$*4*4 = 1040$ channels.
Being the maximum transfer rate between one group of 4 ASAD cards and the corresponding CoBo board equal to $1\,Gb/s$, it is simple to verify that if all channels are fired and read, the maximum rate of the ACQ will be rather small. In fact, let R be the input trigger rate and N_{Ch} the number of fired AGET channels, we have:

$$R(Hz) = \frac{T_{MAX}(Gb) \times 10^9}{(N_{Ch} \times 512 \times 32) + frame_{size}} \,. \tag{3.1}$$

For example, at $R = 1\,kHz$ counting rate and assuming a bandwidth of $1\,Gb/s$, neglecting the frame buffer header dimension, the maximum number of fired channels assumes the value of about $N_{Ch} = 60$. Therefore if all channels are read it is clear that the maximum rate will be much smaller than $100\,Hz$. However, this is not a real limitation in our case, in fact, for comparison, a single particle hitting on a FARCOS telescope can give a maximum multiplicity of 7 channels (front strip 300 micron, front and back strip 1500 micron, CsI signal, and 3 more signal for the double dynamical range for both front signals and CsI). In our recent tests, performed with a "reduced CoBo" board (a standalone limited version of the board) and seven channels readout in the same AGET, an average value of the dead time of $200\,\mu s$ has been measured. This dead time corresponds to a conversion of $7*512$ samples by the same 25 *MHz* ADC and the data transfer towards the reduced CoBo. This dead time is comparable to the dead time of the old CHIMERA ACQ and is totally acceptable.

Chapter 4

Tests of GET electronics with experimental beams

In the previous chapter we have characterized the GET electronics with pulsers and sources. In this chapter we will illustrate the results obtained using GET electronics in several beam tests. We used the new electronics in various configuration set-up and we tested some prototypes of Dual Gain Module.

4.1 Test with ^{7}Li beam

The first test beam, with GET electronics, was made on March 2014. It was used a ^7Li tandem beam at 27.5 MeV on Au, C, plastic, deuterated plastic and LiF targets. It was tested the electronics connected to the FARCOS prototype mounted around zero degree in reduced configuration (see Figure 4.1).

Figure 4.1: Pictures of the set-up used during tests with ^7Li beam.

In particular, telescope number 4 was mounted without Silicon strips to measure, in the CsI(Tl), particles up to Lithium. We show here only the results of one telescope because, due to trigger problems, in this first test we were unable to get good results on $\Delta E - E$ correlation matrix. The standard CHIMERA electronics was also used in parallel to compare the obtained results. Signals were duplicated using a linear fan-in fan-out module. The 4 CsI(Tl) signals were fed to a Silena 761f amplifier giving time and energy signals; the energy was used in the standard CHIMERA electronics, while the time was sent to a CAEN N1568 pulse shape amplifier with CF-discriminator to produce a trigger (delay adapted to CsI). In Figure 4.2 we show the energy spectra obtained from the reaction $^7Li + CH$, CD, and Au, acquired with one of the CsI(Tl) detector coupled with the GET Electronics (left panel) compared with the same detector read with the CHIMERA electronics (right panel).

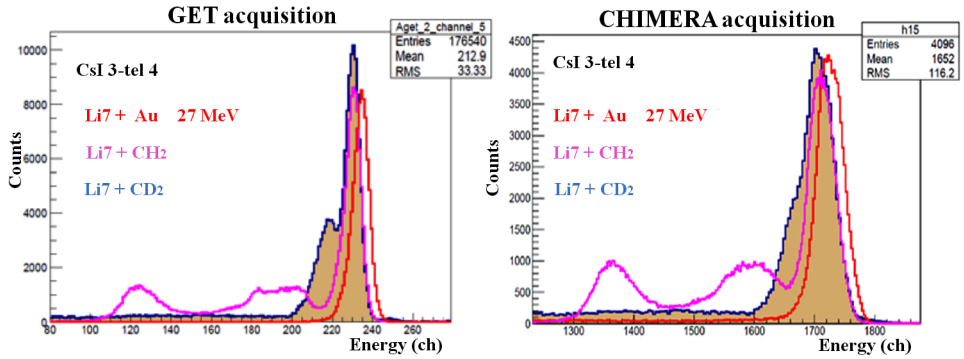

Figure 4.2: Comparison of reactions with different targets from CHIMERA acquisition (right panel) and GET acquisition (left panel).

One can immediately appreciate that the resolution in the case of GET ACQ is better than the standard one. It is possible to notice, in the reaction on the CH target, that the first kinematical solution of elastic scattering on proton target (second violet peak) is much sharper than the one measured with the CHIMERA ACQ. Moreover, in the spectrum collected in the reaction with CD target, elastic peak on deuteron is well seen with the GET ACQ while only a merged two-peak structure in the case of the CHIMERA ACQ is observed. Assuming an average angle of the detector around 6°, the difference in energy between the two peaks is about $800\,keV$. Evidently, part of the peak broadening is due to kinematical spread; therefore, it is not easy to evaluate a precise value for the achieved energy resolution. This acquisition was done using 50 MHz sampling frequency using Gain2 input; the signal was processed with a triangular filter with 180 taps.

4.2 Test with 62 MeV proton beam

Another short beam time was available using 62 MeV proton beams on various targets. The test was performed using GET electronics (reduced CoBo and an Asad Card) on a CHIMERA telescope. With such test it was possible to produce a nice bidimensional histogram using $\Delta E - E$ information (see Figure 4.3).

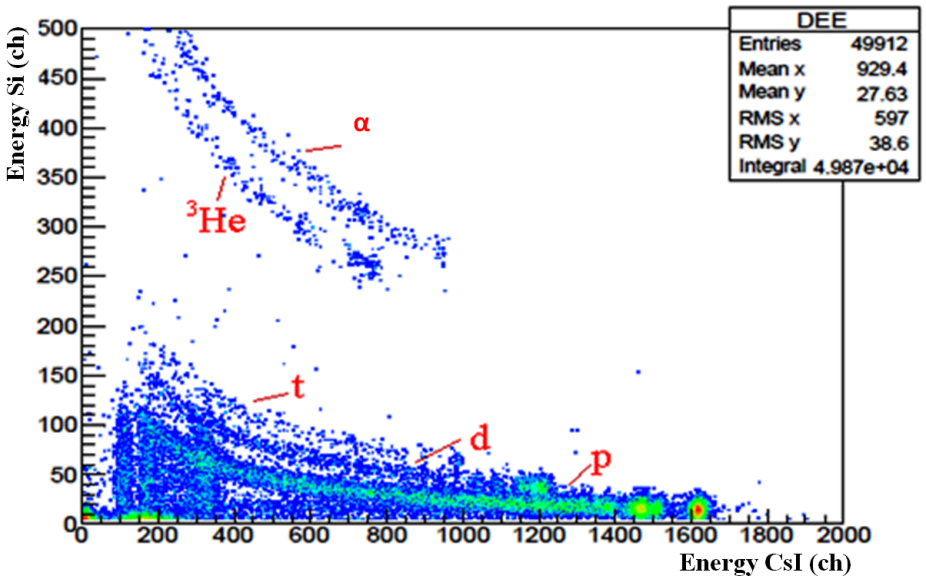

Figure 4.3: $\Delta E - E$ bidimensional histogram in the reaction $p+$ deuterated plastic at 62 MeV. p, d , t, ^3He and α can be clearly identified.

Using only one ASAD card, we digitized both Silicon and CsI(Tl) signals at the same frequency of 25 MHz. This low frequency was chosen in order to collect for a longer time the signal produced in CsI(Tl), and also to better study trigger jitter of the card (we used the ASAD multiplicity trigger). The input of signal was on the SKfilter with small shaping time for CsI(Tl) (220 ns) and a large shaping time for Silicon in order to slow this signal to better match the low frequency of the digitizer. With the larger energy range of particles produced with these reactions, we were able to better explore particle discrimination with fast slow analysis on CsI(Tl). As shown by the good $\Delta E - E$ identification shown in Figure 4.3, this is a quite redundant technique but it can be useful in particular cases in order to discriminate γ-rays.

A rise-time analysis was performed with quite good results as shown in Figure 4.4. Some spread can be seen in the plot around channel 200. It is important to note how slow protons and γ-rays signals are well discriminated. It is of particular importance in this case the correct selection of the trigger delay to digitize the total energy of the particle. The obtained discrimination is good

enough but, however, of lower quality than the one obtained with standard $\Delta E - E$ method.

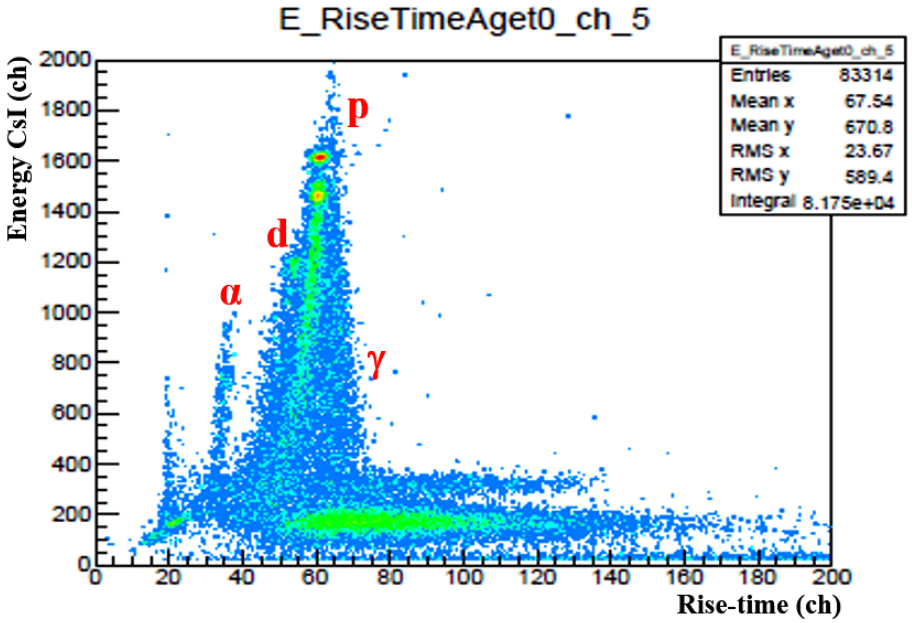

Figure 4.4: Energy vs Rise-time (1 channel = 40 ns) bidimensional histogram obtained in the reaction p+ deuterated plastic at 62 MeV. The helium line is well seen and discrimination between proton, deuterons and γ-rays can be appreciated.

4.3 Test of GET electronics in CLIR experiment

Another check performed with GET electronics was done using one telescope of CHIMERA Ring2 at 4.1° in reactions induced by a CS beam of ^{16}O at 55 $AMeV$ and using a fragmentation beam with ^{6}He, $^{9,8}Li$, $^{10,11}Be$ and other neutron rich projectiles during the experimental campaign CLIR (February-March and June 2015).

As already mentioned, in these experiments we use a Cobo with two ASAD cards. Still the same ASAD card was used for both Silicon and CsI(Tl) signal digitization, so both kind of signals were digitized at 25 MHz and sent to SKfilter input with a shaping time of 1 μs to optimize the signal/noise ratio. In this experiment, the GET internal multiplicity trigger was used.

In Figure 4.5 we see the $\Delta E - E$ identification scatter plot obtained with a $2\,mV/MeV$ gain standard CHIMERA preamplifier for the Silicon stage.

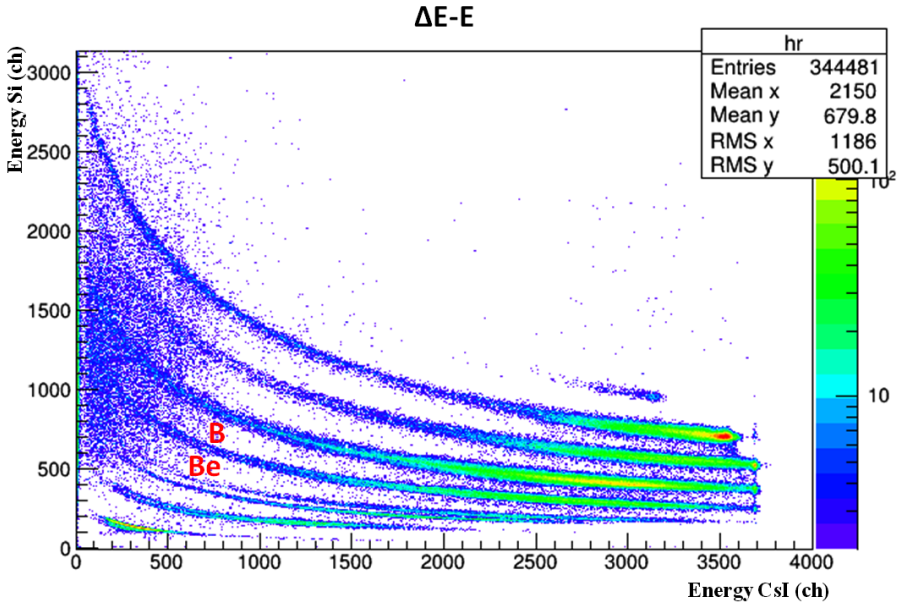

Figure 4.5: Bidimensional histogram obtained with ^{16}O beam at 55 $AMeV$.

Mass identification can be seen up to Be isotopes and at low energy also for Boron isotopes. It is very interesting to see in this reaction the plot Energy vs Rise-time obtained for the CsI(Tl) signals reported in Figure 4.6. This plot is more rich in particles than Figure 4.4 and shows charge discrimination at least up to $Z = 4$.

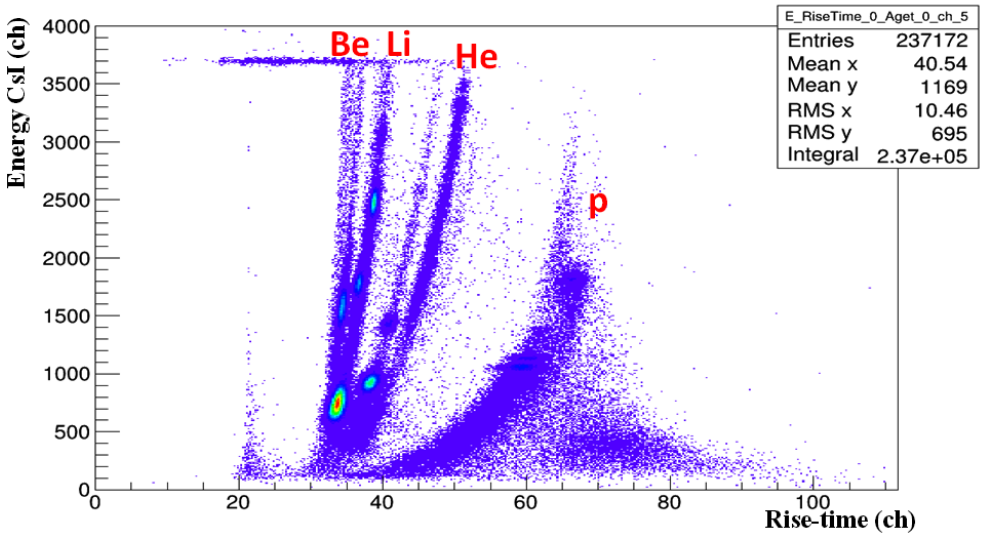

Figure 4.6: Energy vs Rise-time (1 ch = 40 ns for Rise-time) bidimensional histogram in a CsI(Tl) detector with fragmentation beam on a plastic target at 25 MHz sampling frequency.

In this experiment, we got the $\Delta E - E$ bidimensional histogram reported in Figure 4.7 (left panel). The comparison between this bidimensional histogram and the one obtained with classical electronics (right panel) during the UNSTABLE experiment, in the same conditions, shows that using GET electronics we obtain a better isotopic separation at least up to Carbon ions.

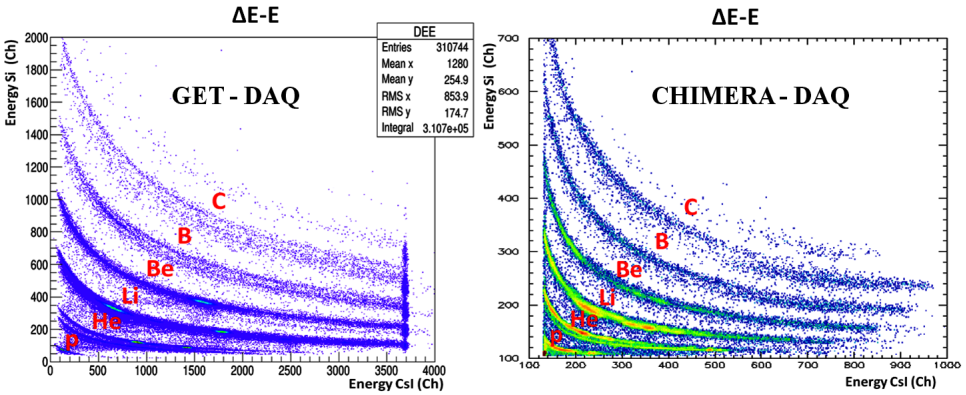

Figure 4.7: Two $\Delta E - E$ bidimensional histograms obtained from the same telescope with GET electronics at 25 MHz sampling frequency during CLIR experiment (left panel) and the standard CHIMERA acquisition during UNSTABLE experiment (right panel). We used fragmentation beams at 50 $AMeV$ on a plastic target in both experiments.

The previous figures shown that good results was obtained using 25 MHz sampling frequency for both Silicon and CsI(Tl) detector. In the same experiment we also evaluated the possibility to use 50 MHz sampling frequency for GET acquisition. As already mentioned, this is the best compromise between fast Silicon signals (which should be sampled at 100 MHz) and the slower signals of CsI (Tl) (which should be sampled at 25 MHz). However, at the time of this experiment we were unable to use two CoBo so only one frequency could be used. The obtained $\Delta E - E$ bidimensional histogram is reported in Figure 4.8:

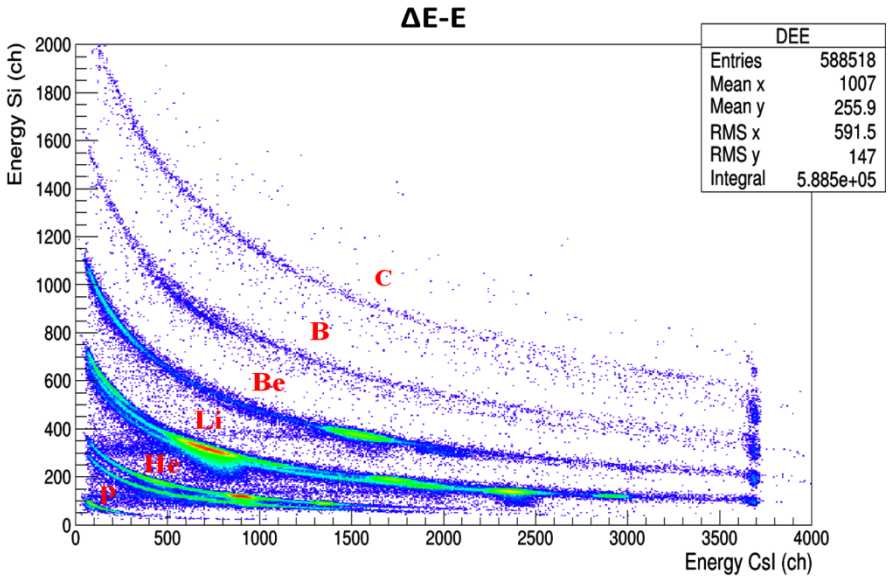

Figure 4.8: $\Delta E - E$ bidimensional histogram obtained from the same telescope with GET electronics at 50 MHz sampling frequency during CLIR experiment. We used fragmentation beams at 50 $AMeV$ on a plastic target.

At 50 MHz the bidimensional histogram seems even better than at 25 MHz even if a more detailed analysis is necessary in order to extract the charge and mass resolution. Both frequencies gives relatively good results from the point of view of the energy resolution. In addition, pulse shape analysis is also good at 50 MHz as shown in Figure 2.16; however, as shown in paragraph 3.9 higher frequency is better from the point of view of timing resolution. In CLIR experiment, we tested, for the first time, a prototype of Dual Gain Module (Figure 4.9) with a single input and an output of gain $\times 1$, in order to verify its DC offset and linearity response.

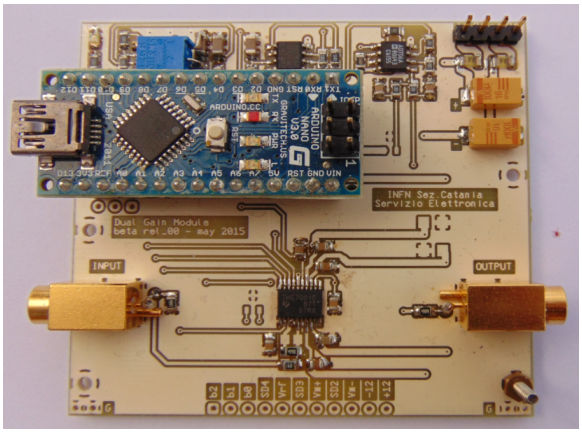

Figure 4.9: Photo of the first prototype of Dual Gain Module used during CLIR experiment.

In this case, we have duplicated the signal coming out from CsI(Tl) preamplifier. A copy of signal was sent, with external DC offset, to a SKfilter input channel of GET electronics with a shaping time of 1 μs, while the other one was sent, without external DC offset, to prototype of Dual Gain Module and then, to SKfilter input channel of GET electronics with the same set-up of the first one. We obtained the two $\Delta E - E$ shown in Figure 4.10:

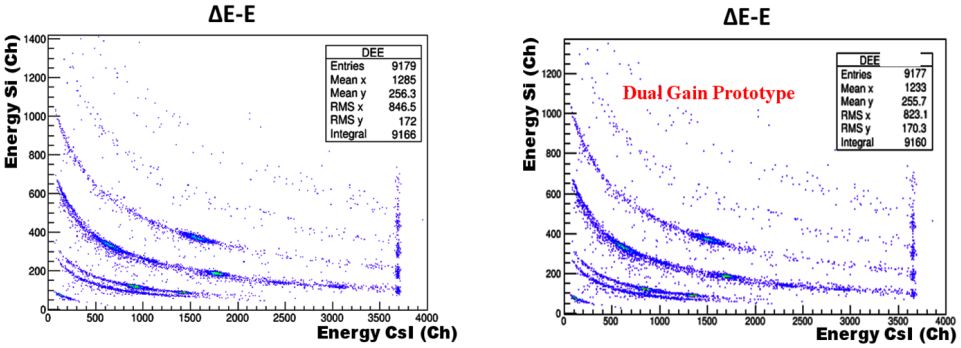

Figure 4.10: Comparison between $\Delta E - E$ bidimensional histograms obtained with (right panel) and without (left panel) a Dual Gain prototype.

The comparison shown that, practically, we get the same result. The development of the prototype was then continued, as we shall see later.

4.4 GET-CHI test

In May 2016, we have conducted more tests on GET electronics using both CS beam ^{16}O at 50 $AMeV$ and proton beam (for the calibration) at 19.7 MeV on Al, $Au + LiF$, C, CH_2 and CD_2 targets. In these tests, we used a CoBo with 4 ASAD cards. To get a good trigger in this condition it was necessary to put aluminum shields for the 4 ASAD cards, as shown in Figure 4.11:

Figure 4.11: ASAD cards with aluminum shields. These provisional shields will be replaced by the ones shown in Figure 3.12.

We used various telescopes of CHIMERA multi-detector, in particular the telescopes of Ring2 N°6-I and N°18-E , Ring10 N°10 and N°24 , Ring13 N°24 and Ring14 N°18. Both Silicon and CsI(Tl) were digitalized at 50 MHz frequency and sent to SKfilter input with a shaping time of 502 ns.
During this test, the prototype of Dual Gain Module was not available, however we were able to increase the dynamic range of GET electronics using an interesting induction effect. We in fact noticed that, using Skfilter or Gain2 input mode, induced signals are generated on the channels nearest to the one used, if they are not terminated. In Figure 4.12, we show the induction generated on channel 8 by a signal on channel 7. We were not

worried by this induction because it was generated on open (not connected) channels (in this case channel 8) while in a terminated channel the maximum measured induction is of the order of $1-2$ channels with a saturated signal.

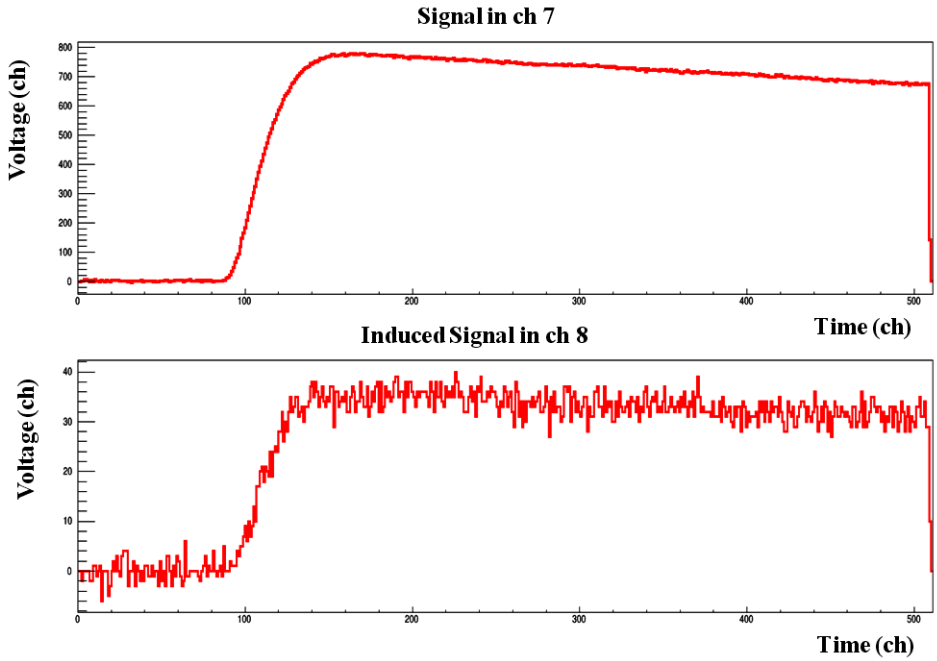

Figure 4.12: Signal in SKfilter input (top panel) with maximum of about 800 channels and induced signal in channel 8 (bottom panel) with maximum of about 40 channels corresponding to 5 % of signal.

No induction can be appreciated for reasonable signals. Looking in detail to the induction signal (Figure 4.12) one see that this signal is just an attenuated reply of the input one saving all input characteristics apart the height. We did some check on the linearity of this signal in order to verify if it can be used to extend the dynamical range of GET electronics. In effect, as shown in Figure 4.13 and Figure 4.14, the induced signal follow with rather good linearity the input signal.

There is no change in the shape of the induced signal when the input signal goes to saturation and so we used this signal to extend the dynamical range of ASAD in case of use of external preamplifier like in these tests. In this experiment we used the induced signals to study kinematical coincidences using CHIMERA telescopes and so check this effect.

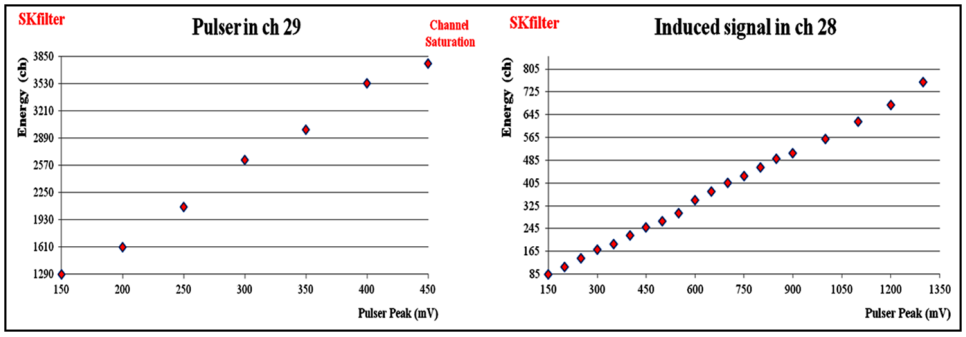

Figure 4.13: Trend of maximum of signal (left panel) and of maximum of induced signal (right panel) for SKfilter input.

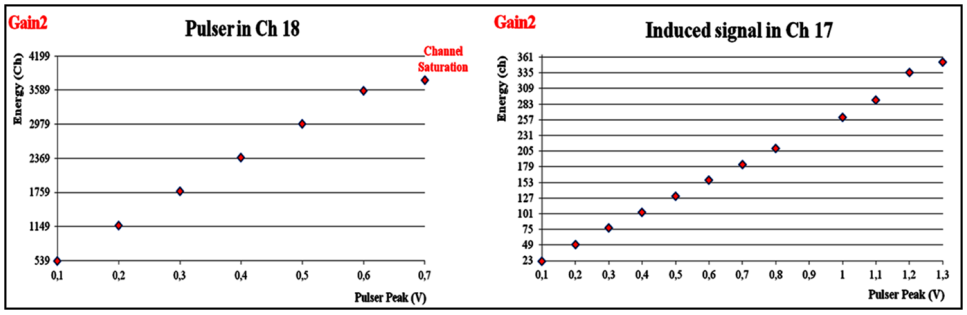

Figure 4.14: Trend of maximum of signal (left panel) and of maximum of induced signal (right panel) for Gain2 input.

In particular we have investigated the kinematical coincidences between ^{16}O at 50 $AMeV$ detected in CHIMERA telescope N°6-I of the Ring2 and proton detected in CHIMERA telescope N°24 of the Ring13. These protons are produced in the scattering of ^{16}O on target of CH_2. Events were selected, searching for ^{16}O coincidences in Ring2 N°6-I (induced signals for CsI(Tl)) with protons detected in the Ring13 N°24. These detectors were chosen according to kinematics. In fact, taking in account momentum conservation, the relative azimuthal angle $\Delta\varphi$ between the two telescopes must be 180°. In Figure 4.15 we show the total energy (the energy loss in Silicon summed at the energy detected in CsI(Tl)) of particles stopped in telescope N°6-I of Ring2 (induced signals for CsI(Tl) are considered in this case) while the Figure 4.16 shows the total energy of particles stopped in telescope N°24 of Ring13. In both telescopes we have selected only the events detected in

coincidences in the two telescopes.

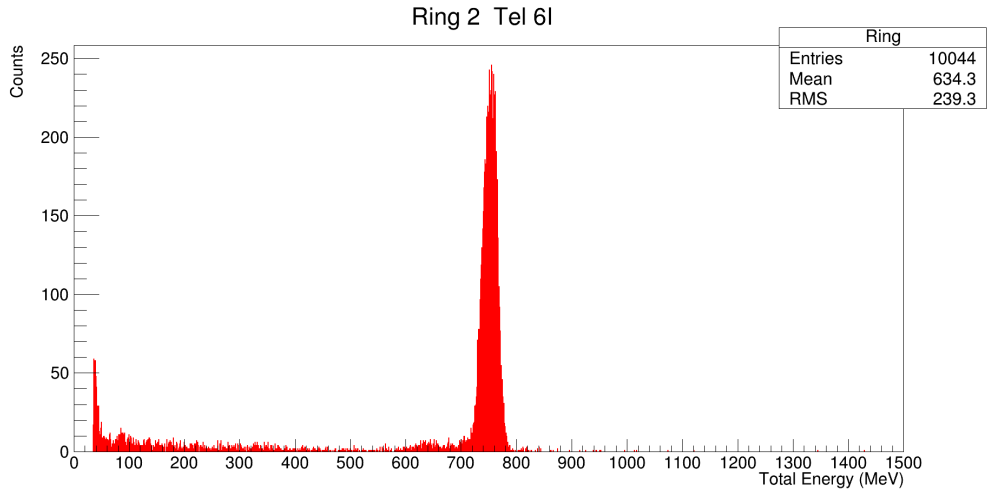

Figure 4.15: Total energy of particles detected on telescope N°6-I of the Ring2 in reaction $^{16}O + CH_2$. In this case we considered the induced signals for CsI(Tl) and only the events in coincidences with a particle detected in the telescope N°24 of the Ring13.

The previous plot shows a peak at around 750 MeV that corresponds to the total energy of ^{16}O in coincidences with protons in Ring13 N°24. Spurious coincidences are shown at low energies near to the pedestal.

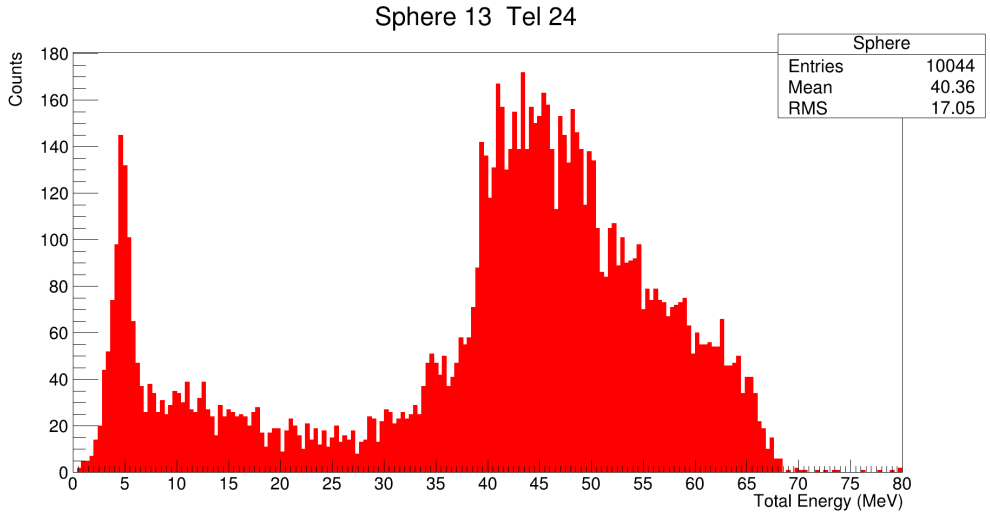

Figure 4.16: Total energy, in reaction $^{16}O + CH_2$, of the particles detected on telescope N°24 of the Ring13 and in coincidence with the ones in the telescope N°6-I of the Ring2.

The plot of Figure 4.16 shows a peak at around 5 MeV due to spurious events and a range of energy from 30 to 60 MeV corresponding to protons in coincidences with ^{16}O in Ring2 N°6-I.
In Figure 4.17 the previous results are grouped into a single scatter plot. This plot shows better the coincidences between ^{16}O and protons. Even if the energy resolution of CsI(Tl) is not enough to discriminate elastic scattering and inelastic excitation, a kinematic coincidence line is well seen evidenced by the red circle.

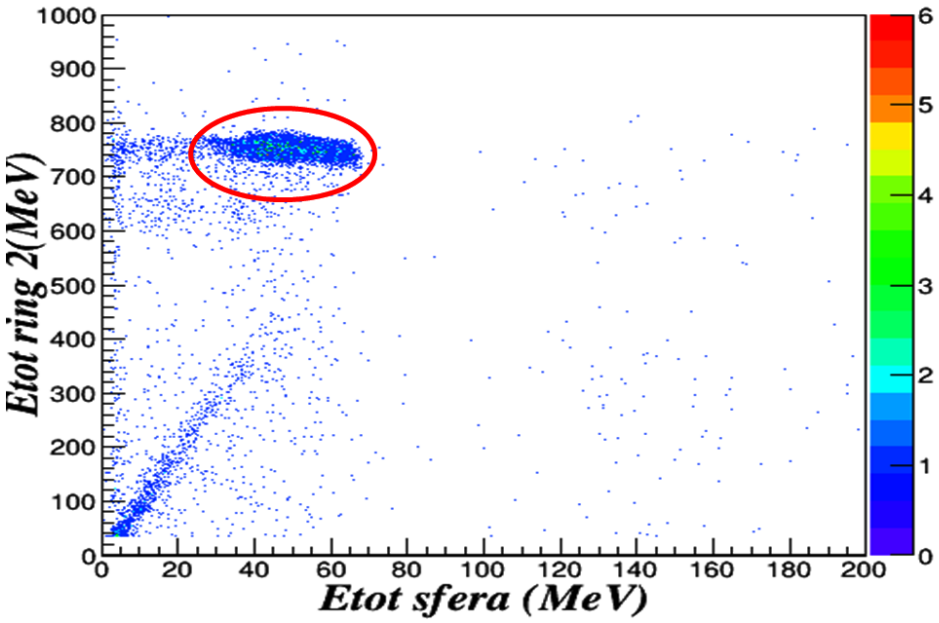

Figure 4.17: Bidimensional histogram of energy measured by couple of telescopes in coincidence.

The total detected energy obtained summing the energies in the two detectors is shown in Figure 4.18. Again resolution is not enough to discriminate elastic and inelastic scattering however the result evidence the good linearity of the induction signal. We note that due to kinematical relations, from the proton energy spectrum of Figure 4.16, as shown in [43], one can extract an angular distribution in the Center of Mass system with beautiful angular resolution of the order of 1°.

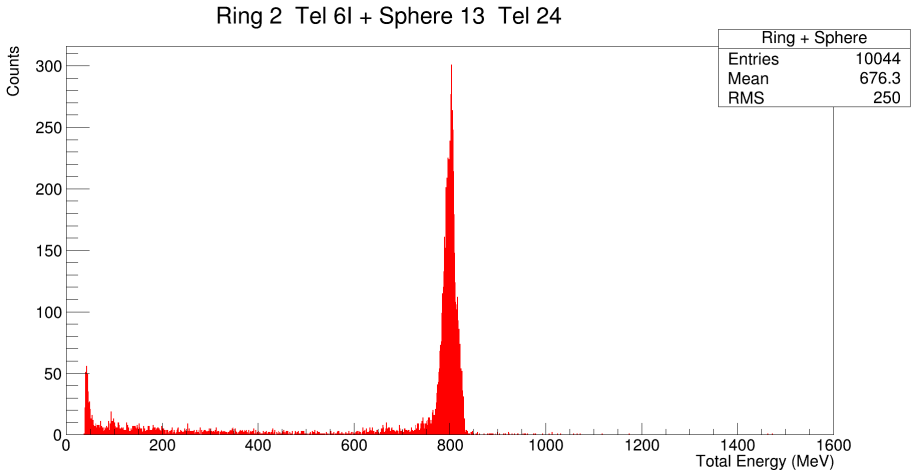

Figure 4.18: Total energy of two coinciding telescopes.

4.5 BARRIERS Experiment

Another test of GET electronics was conducted during Barriers experiment. In this experiment a tandem beam of ^{24}Mg was used to measure the barrier distribution for the reactions $^{24}Mg + {}^{90,92}Zr$. In this experiment, we used a second prototype of Dual Gain Module shown in Figure 4.19:

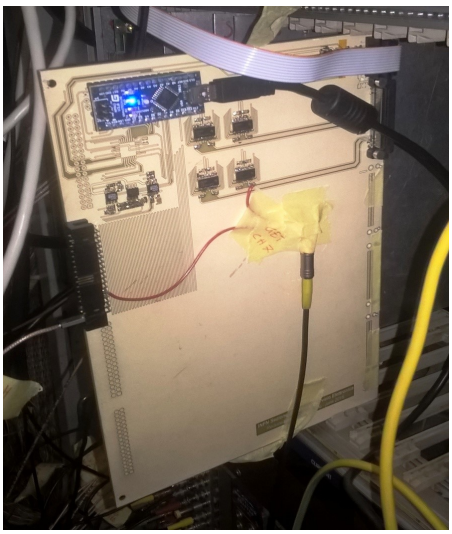

Figure 4.19: Photo of second Prototype of Dual Gain Module.

This prototype has four inputs. To each input corresponds two outputs

to which you can give a different offset and gain ($\frac{1}{8}$, $\frac{1}{4}$, $\frac{1}{2}$, 1, 2, 4, 8). We tested the prototype for many values of offset and for the possible gains in order to check the behavior of the prototype in stress conditions. The test was in fact performed using a fast scintillator, so testing also the band filter of the dual gain module. We obtained good quite results as shown in Figure 4.20:

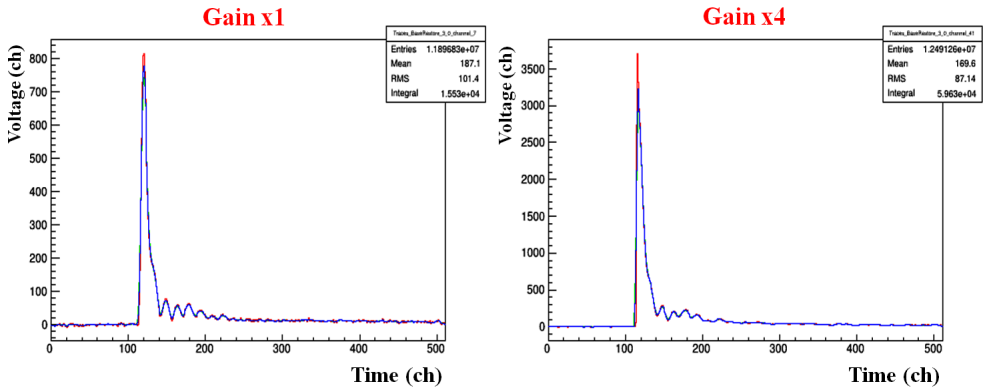

Figure 4.20: Example of digital waveforms obtained with the second prototype of Dual Gain module.

In this case in left panel we can see a signal with a gain $\times 1$ and in right panel the same signal with gain $\times 4$; both signals were acquired with the same offset of $800\,mV$.
Figure 4.20 shows that different gain of prototype not introduced significant variations in the signal shape.

The signals of the previous figure were generated in an EJ $299-33$ plastic scintillator. This detector was tested with the aim to proof its quality in particle and neutron detection and identification. In this experiment, we used GET electronics (4 ASAD cards shielded like in GET-CHI test). The employed scintillator is characterized by fast charge collection time therefore we used the signals in SKfilter stage with 100 MHz sampling frequency and shaping ($70\,ns$). Plastic scintillators play important role in detection of nuclear radiation [44] since the dawn of nuclear research. They have several beneficial properties including the ease of machining and a relatively low cost per volume, which makes them useful in many practical applications. However, unlike select liquid or crystalline scintillators, until recently, they

lacked the pulse-shape discrimination capability needed in the applications where neutrons are to be measured in the presence of radiation. The latter drawback is now gone with a commercial release of a new type of plastic scintillator by Eljen Technology [45] named EJ $299-33$. The detector telescope including the EJ $299-33$ scintillator of interest was placed at approximately $1.2\,m$ from the target at an angle of approximately $5°$ (see Figure 4.21).

Figure 4.21: The experimental set-up for the test of the EJ $299-33$ plastic scintillator. The scintillator coupled to photomultiplier covered by black plastic can be observed between Ring9 and the sphere of CHIMERA.

The scintillation detector assembly consisted of a $5\,cm$ by $5\,cm$ cylindrical EJ $299-33$ plastic, optically coupled to the photocathode of a Hamamatsu R7724 photomultiplier tube characterized by a spectral response range from 300 to $650\,nm$, all operated under high vacuum. The photomultiplier tube was operated at $1.6\,kV$ of anode voltage supplied via a base model VD23N-7724, also by Eljen Technology [45].
The anode signal of the Hamamatsu phototube was sent to the prototype of Dual Gain Module and so to GET electronics. This was a real stress test for the GET electronics showing that even with very fast signals one can obtain quite good results. The availability of the digitized signal allow to analyze

many kind of pulse shape in order to study pulse shape discrimination. Various gate with different length were used in order to perform a fast-slow analysis of the signal. An example of this analysis is shown in Figure 4.22.

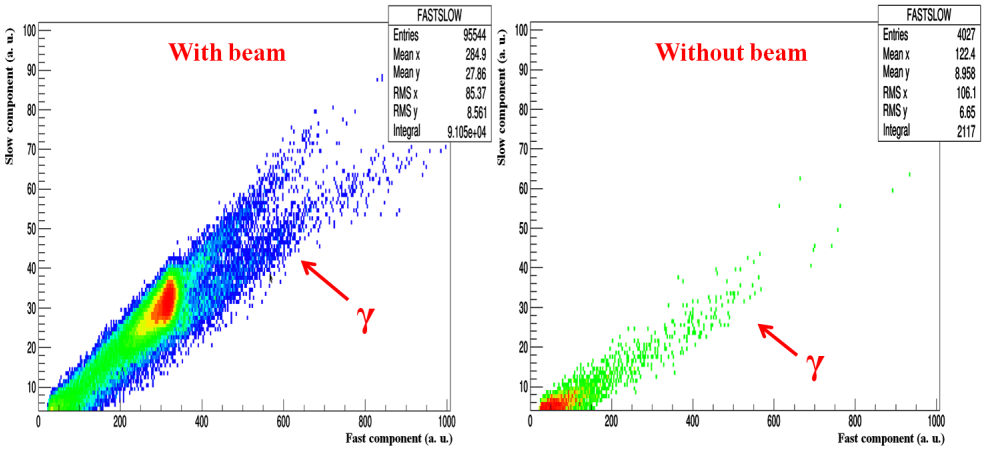

Figure 4.22: Example of fast-slow scatter plot generated in a reaction of $^{24}Mg + {}^{90}Zr$ at 72 MeV (left panel) and without beam (right panel). In left panel two lines can be observed. The lowest one is due to gamma and cosmic rays. The upper line is due to the detection of other particles produced in the reaction. In this line the bump of elastic scattering can be observed.

Two lines can be observed in the Figure 4.22 (left panel). The upper line is due to the detection of other particles produced in the reaction. The elastic scattering events of ^{24}Mg are evidenced as a bump. The lowest one is the line of relativistic particles, gamma rays, electrons. This line is better evidenced in right panel that was collected in a run without beam, so when only cosmic ray and gamma rays from radioactivity are detected. The neutron-gamma discrimination was further tested and optimized, with the same apparatus using various sources and in particular an $Am - Be$ source for the neutron production that can be seen in Figure 4.23.

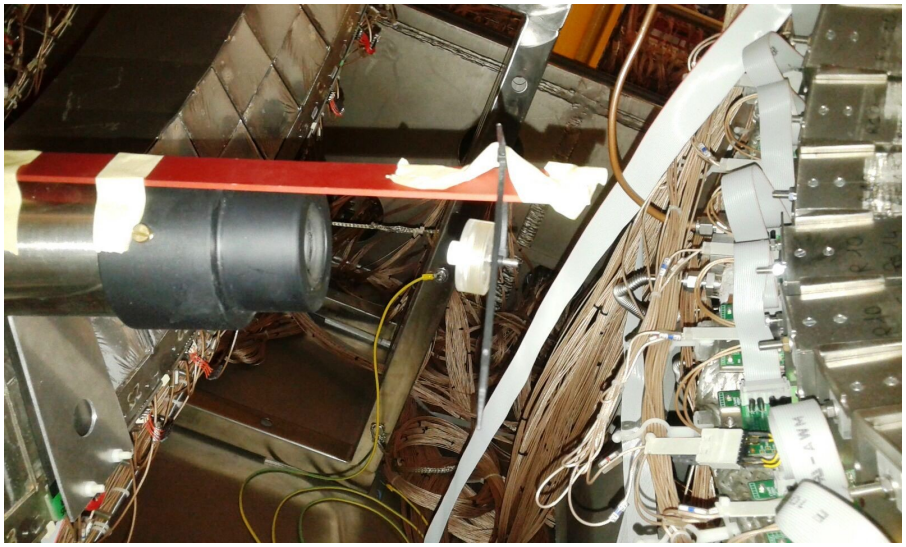

Figure 4.23: The experimental set-up for the test of the EJ $299-33$ plastic scintillator. The scintillator coupled to photomultiplier covered by black plastic can be observed between Ring9 and the CHIMERA sphere. Also the $Am-Be$ and ^{60}Co sources put in front of it can be noted.

As shown in Figure 4.24 we obtained very good results changing the gate of fast-slow component. This fact confirm the advantage of GET electronics, in fact offline we can change the parameters of the analysis adapting in the better way to specific physics cases.

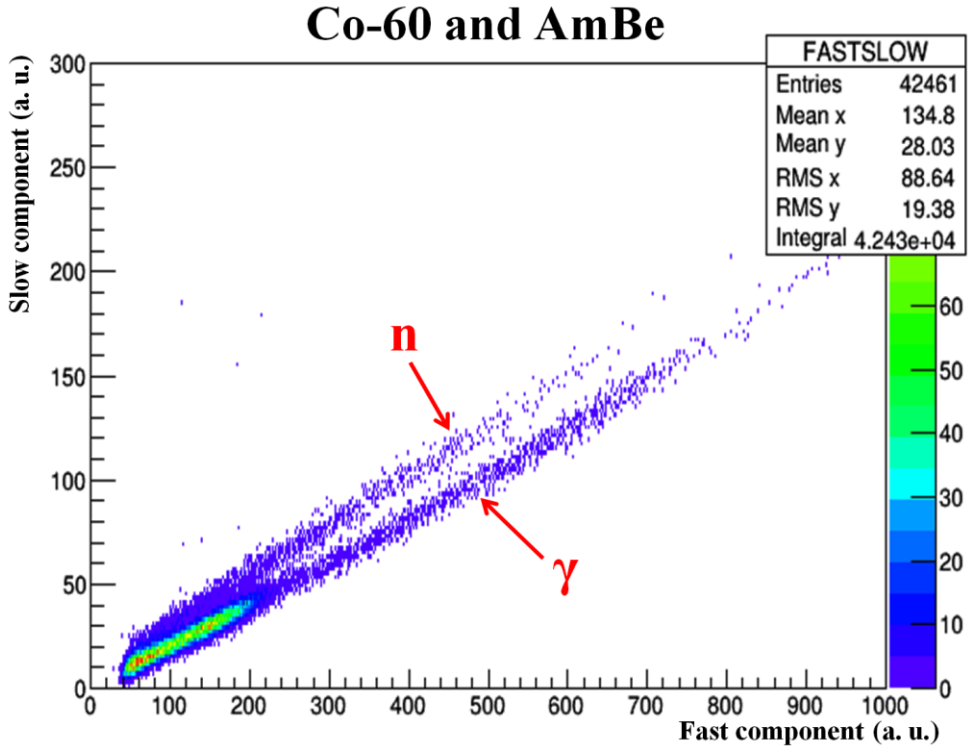

Figure 4.24: Fast-slow scatter plot obtained during tests with ^{60}Co and $Am - Be$. In this case we are able to discriminate γ from n particles.

Conclusions

We characterized the performance of GET electronics and evaluated the feasibility of its use for the readout of the CHIMERA and FARCOS telescopes. The possibility to choose the stage input for external signals allows us to use our PA, designed in the best way for CHIMERA and FARCOS telescopes, coupled with the SKfilter stage of GET electronics. Thanks to SKfilter stage we can improve the signal/noise ratio. Moreover, the possibility of changing the peaking time of SKfilter stage (from $70\,ns$ to $1\,\mu s$) made possible to better adapt the GET electronics to the signal shapes as seen in various beam tests described in chapter 4. In chapter 3 we have seen the excellent results in the linear response of GET electronics. This last aspect, the reduction of power dissipation and the decrease in size of the GET electronics (an ASAD card is as large as a VME card) make the system transportability easier in other laboratories. Therefore, as seen in chapter 3, we could use the new electronics at the University of Messina coupled with a Germanium detector and thanks to the excellent energy resolution of the Germanium scintillator we were able to verify the intrinsic quality of GET electronics. We obtained an energy resolution of 0.2 %, to be compared with 0.1 % measured with MAESTRO ACQ system, therefore we conclude that the intrinsic resolution of GET electronics is of the order of 0.2 %. In chapter 3 we also illustrated the results obtained testing GET electronics on several CHIMERA and FARCOS detectors with various sources. In the test with ^{60}Co we have seen that thanks to prototype of the Dual Gain Module we are able to discriminate also gamma rays with low energy (with standard acquisition we have a threshold of $2-3\ MeV$ and we are not able to discriminate gamma rays with low energy). Moreover the studies on the numerical filters used to determine

the signal amplitude (chapter 3) showed us that it is possible to improve CsI(Tl) and Silicon resolution. Regarding the Silicon channel we observe that a beautiful energy resolution can be attained allowing satisfying isotopic identification also at very low released energy (the energy loss of 62 MeV proton in Silicon is only 500 keV).
In order to solve the problem of the limited dynamic range we have seen that it is enough to use two GET readout channels per detector readout channel. We have seen that the use of prototypes of Dual Gain Module give us encouraging results but also considering the induced signals (chapter 4) we could extend the dynamic range of GET electronics. Moreover another advantage of digital acquisition is the fact that pedestal is measured event by event (by measuring the baseline of the preamplifier signal) and, consequently, subtracted improving the energy resolution. Therefore the fit calibration line must intercept the zero and small nonlinearities characterizing CsI(Tl) can be easily measured. The studies (chapter 3) on time resolution and on dead time showed very good results. With GET electronics we obtained a time resolution of about 100 ps better than the CHIMERA ACQ (the TDC step in CHIMERA is 250 ps) while for the dead time we obtained 200 μs for GET, comparable to the dead time of the old CHIMERA ACQ. GET electronics was also tested with fast detectors as the new plastic neutron detector EJ $299-33$ (chapter 4).
Finally, we had seen that we are able to acquire with low multiplicity screening the ASAD cards. Therefore, we conclude that the GET electronics is a very good choice for the CHIMERA and FARCOS electronics. These very beautiful results push us to extend also to the readout of CHIMERA Silicon detector the digital GET electronics.

Bibliography

[1] B. Li, G. Verde, A. Ramos, I. Vidana, Nuclear Symmetry Energy, Topical Issue, Europan Physics Journal A50, 2 (2014).

[2] E. De Filippo and A. Pagano, Eur. Phys. J. A 50, 32 (2014), P. Russotto et al., Phys. Rev. C 91, 014610 (2015), E. De Filippo et al., Acta. Phys. Pol. B 40, 06011 (2009), G. Cardella et al., Phys. Rev. C 85, 064609 (2012), G. Cardella et al., Nucl. Instr. Meth. A 799, 64 (2015), D. Dell'Aquila et al., Phys. Rev. C 93, 024611 (2016).

[3] A. Pagano et al., Nuclear Physics. A 681, 331 (2001).

[4] M. Alderighi et al., "Particle identification via pulse shape analysis for large- area silicon detectors of the CHIMERA array", Report IEEE: Institute of Electrical and Electronic Engineers. Transactions on Nuclear Science Volume: 52, Issue: 5 (2005).

[5] A. Pagano et al., "Fragmentation studies with the CHIMERA detector at LNS in Catania: Recent progress", Nucl. Phys. A, vol. 734, pp. 504511, 2004.

[6] G. Verde et al., "The Farcos project: Femtoscope Array for Correlations and Femtoscopy", Journal of Physics: Conference Series, vol. 420, no. 012158, pp. 18, 2013.

[7] G. Verde, A. Chibibi, R. Ghetti, R. Helgesson, "Correlations and Characterization of Emitting sources", Eur. Phys. J. A, vol. 30, pp. 81108, 2006.

[8] G. Verde, "Particle-Particle Correlations: Femtoscopy and Tools for Spectroscopy", EPJ Web of Conference, vol. 31, no. 00033, pp. 112, 2012.

[9] L. Acosta et al., EPJ Web of Conferences 31 00035 (2012), G. Verde et al., Journal of Physics: Conference Series 420 (2013) 012158, L. Quattrocchi et al., EPJ Web of Conferences 66 11001 (2014), E.V. Pagano et al, EPJ Web of Conferences 88, 00013 (2015).

[10] J. Pounthas et al., NIM A357, 418 (1995).

[11] F. Gramegna et al., NIM A 389, 474 (1997).

[12] R. Bougault et al., Eur. Phys. J. A 50, 47 (2014).

[13] E. Pollacco et al., Eur. Phys. J. A 25, s01, 287288 (2005).

[14] A. Cunsolo et al., NIM A 481 48 (2002).

[15] S. Szilner et al., Phys. Rev. C 76, 024604 (2007).

[16] S. Pullanhiotan et al., Nucl. Instr. And Meth. A 593, 343 (2008).

[17] G. Verde et al., Eur. Phys. J. A 30, 81 (2006).

[18] E. De Filippo et al., Phys. Rev. C 86, 014610 (2012).

[19] V. T. Jordanov and G. F. Knoll, Nucl. Instr. And Meth. A 345, No. 2, pp. 337345, (1994).

[20] J. Kemmer, Nucl. Instr. and Meth. A, 226:89, 1984.

[21] S. Aiello et al., Nucl. Instr. and Meth. A, 369:50, 1996.

[22] F. Amorini et al., IEEE Trans. Nucl. Sci., 59, N. 4, 2012.

[23] F. Amorini et al., IEEE Trans. Nucl. Sci., 55 No. 2 (2008), 717-722.

[24] M. Alderighi et al., Nucl. Phys. A, 734:E88-E91, 2004., M.Alderighi et al. IEEE Trans Nucl. Sci., 52:1624, 2006.

[25] S. Aiello et al., IEEE Trans. Nucl. Sci., 45:1798, 1998.

[26] S. Aiello et al., IEEE Trans. Nucl. Sci., 45:1877, 1998.

[27] S. Aiello et al., Nucl. Instr. and Meth. B, 136:1172, 1998.

[28] S. Aiello et al., IEEE Trans Nucl. Sci., 47:114, 2000.

[29] S. Aiello et al., IEEE Trans Nucl. Sci., 47:196, 2000.

[30] M. Alderighi et al., IEEE Trans. Nucl. Sci., 49:432, 2002.

[31] A. Alderighi et al., IEEE Trans. On Nucl. Sci., 52:1624, 2005.

[32] http://www.thorlabs.com/newgrouppage9.cfmobjectgroup_$id = 7616$.

[33] E. Pollacco et al., Phys. Procedia 37, 1799 (2012).

[34] VT893 μTCA crate, produced by Vadatech: www.vadatech.com.

[35] L. Acosta at al., IEEE Trans Nucl. Sci., 60 (volume) (2013) 284-292.

[36] C. A. J. Ammerlaan et al., Nucl. Instr. and Meth., 22:189200, 1963.

[37] J. B. A. England et al., Nucl. Instr. and Meth. A, 280:291, 1989.

[38] M. Alderighi et al., IEEE Trans. On Nucl. Science 52, 1624 (2005); ibid. IEEE Trans. On Nucl. Science 53, 279 (2006).

[39] X. Grave et al., Proceedings of the Real Time Conference 2005, 14th IEEE-NPSS, pag. 5 (2005). doi: 10.1109/RTC.2005.1547454.

[40] SOAP (Simple Object Access Protocol) is a protocol for exchanging structured information through the Web using the XML technology. It is also widely used by all the software tools for GET Electronics, in particular for the slow control setup procedures.

[41] The Run Control Core (RCC) is part of the GANIL data acquisition. It includes a GUI interface mainly written in Java. See: http://wiki.ganil.fr/gap/.

[42] Bardelli et al., Nuclear Instruments and Methods in Physics Research A 521 (2004) 480492; F. Amorini et al., IEEE Transaction on Nuclear Science, 55 (2008) 717-722.

[43] L. Acosta et al., NIM 715 (2013) 56-61.

[44] G. Knoll, Radiation Detection and Measurement, John Wiley & Sons, Inc, 2000.

[45] Eljen Technology, http://www.eljentechnology.com/.